Published in final edited form as:

Mol Cell. 2022 December 01; 82(23): 4548–4563.e4. doi:10.1016/j.molcel.2022.10.008.

Structural insights into assembly and function of GluN1-2C, GluN1-2A-2C, and GluN1-2D NMDARs

Tsung-Han Chou[1], **Hyunook Kang**[1], **Noriko Simorowski**[1], **Stephen F. Traynelis**[2], **Hiro Furukawa**[1,3,*]

[1]W.M. Keck Structural Biology Laboratory, Cold Spring Harbor Laboratory, Cold Spring Harbor, NY 11724, USA.

[2]Department of Pharmacology and Chemical Biology, Emory University School of Medicine, Atlanta, GA 30322, USA.

[3]Lead contact: Hiro Furukawa

Summary

Neurotransmission mediated by diverse subtypes of *N*-methyl-D-aspartate receptors (NMDARs) is fundamental for basic brain functions and development as well as neuropsychiatric diseases and disorders. NMDARs are glycine and glutamate-gated ion channels that exist as heterotetramers composed of obligatory GluN1 and GluN2(A-D) and/or GluN3(A-B). The GluN2C and GluN2D subunits form ion channels with distinct properties and spatio-temporal expression patterns. Here, we provide the structures of the agonist-bound human GluN1-2C NMDAR in the presence and absence of the GluN2C-selective positive allosteric potentiator (PAM), PYD-106, the agonist-bound GluN1-2A-2C tri-heteromeric NMDAR, and agonist-bound GluN1-2D NMDARs by single-particle electron cryomicroscopy. Our analysis shows unique inter-subunit and domain arrangements of the GluN2C NMDARs, which contribute to functional regulation and formation of the PAM binding pocket and is distinct from GluN2D NMDARs. Our findings here provide the fundamental blueprint to study GluN2C- and GluN2D-containing NMDARs, which are uniquely involved in neuropsychiatric disorders.

Graphical Abstract

[*]Corresponding Author: Hiro Furukawa, furukawa@cshl.edu.

Author Contributions

T-H.C., H.K., and H.F. designed and conducted experiments involving cryo-EM and electrophysiology. N.S. made DNA constructs and conducted initial characterization of the GluN1a-2C NMDAR proteins. S.T. conducted electrophysiology on the GluN1a-N368Q mutant. T-H.C., H.K., S.T., and H.F. wrote the manuscript.

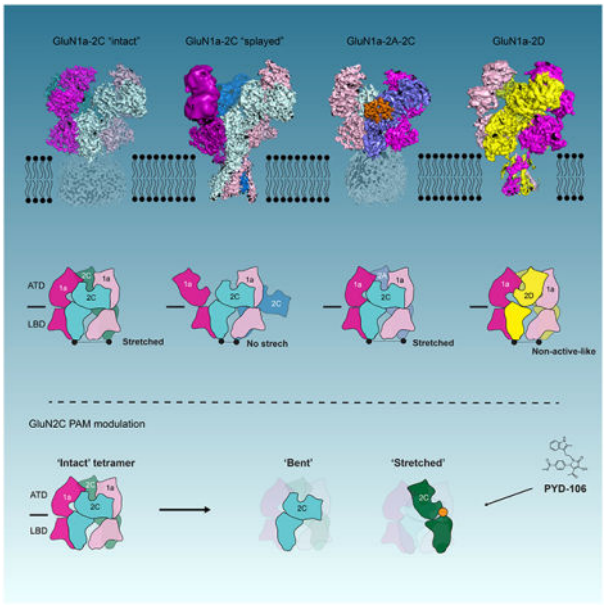

eTOC Blurb

The structures of GluN1-2C, GluN1-2A-2C, and GluN1-2D NMDARs presented in this study revealed unique assembly patterns that form ion channels with distinct functional properties.

Keywords

GluN1-2C NMDA receptor; GluN1-2A-2C triheteromeric NMDA receptor; GluN1-2D NMDA receptor; allosteric modulation; PYD-106; single-particle cryo-EM

Introduction

NMDARs elicit diverse patterns of neuronal signaling in response to glutamate transmission by forming a number of distinct heterotetrameric channels between the obligatory GluN1 subunit and a broad spectrum of GluN2 (A-D) and GluN3 (A-B) subunits (Hansen et al., 2021). These different subtypes of NMDAR channels display distinct patterns of ion channel activities, pharmacology, and spatio-temporal expression, which are pivotal to basic brain functions and development (Hansen et al., 2021; Hansen et al., 2018). Dysfunctional NMDARs are implicated in a wide variety of neurological and neuropsychiatric conditions including schizophrenia, depression, stroke, Alzheimer's disease, and seizure (Hansen et al., 2021; Paoletti et al., 2013). The GluN2C subunit is expressed postnatally in discrete regions, such as cerebellar granule cells (Akazawa et al., 1994; Lu et al., 2006; Takahashi et al., 1996), spinal cord (Akazawa et al., 1994; Allgaier et al., 2001), and cortical interneurons (Belforte et al., 2010; Korotkova et al., 2010; Ravikrishnan et al., 2018). The GluN2D subunit shows widespread expression in early brain development but becomes restricted to selected neurons such as interneurons in the hippocampus, cortex, thalamus, basal ganglia and cerebellum in adult brains (Akazawa et al., 1994; Monyer et al., 1994; Salimando et al., 2020). The GluN2C and GluN2D differ in their expression pattern compared to GluN2A

and GluN2B, both of which show strong and broad expression in cortex, hippocampus, and other regions (Paoletti et al., 2013). The functional properties of the GluN1-2 NMDARs can be clustered into two groups: GluN1-2A/GluN1-2B and GluN1-2C/GluN1-2D where GluN1-2A/GluN1-2B NMDARs show higher potency of Mg^{2+} block, Ca^{2+} permeability, single-channel conductance, and open probability than the GluN1-2C/GluN1-2D NMDARs (Cull-Candy and Leszkiewicz, 2004; Dravid et al., 2008; Siegler Retchless et al., 2012). Consistently, GluN2A and GluN2B have higher sequence identity with each other than with GluN2C and GluN2D. The GluN2C-containing NMDARs have little or no desensitization (Traynelis et al., 2010) and low sensitivity to extracellular pH (Traynelis et al., 1995).

Mechanistic understanding of GluN2C- and GluN2D-containing NMDARs has lagged behind that of GluN2A- and GluN2B-containing NMDARs (Chou et al., 2022; Chou et al., 2020; Jalali-Yazdi et al., 2018; Karakas and Furukawa, 2014; Lu et al., 2017; Regan et al., 2018; Song et al., 2018; Tajima et al., 2016; Tajima et al., 2022; Wang et al., 2021; Zhang et al., 2018; Zhang et al., 2021; Zhu et al., 2016) due to the complete lack of structural information of GluN2C and the limited information of GluN2D stemming from a technical difficulty in protein production. The only currently available structural information for the GluN2C/2D group is on the isolated ligand-binding domains (LBDs) of GluN2D and GluN2C/D-mimetic constructs (Hansen et al., 2013; Vance et al., 2011; Wang et al., 2020). Here we address these shortfalls by providing the structures of the agonist-bound human GluN1a-2C NMDARs in the presence and absence of the GluN2C-specific positive allosteric modulator (PAM), PYD106, the human GluN1a-2A-2C tri-heteromeric NMDARs, and the human GluN1a-2D NMDARs.

Results

The structure of GluN1a-2C di-heteromeric NMDAR

To gain structural insights into the GluN2C subunit, we implemented single-particle cryo-EM on the human GluN1a-2C NMDAR. Here, the carboxy-terminal domain (CTD) was truncated from the GluN2C subunit as in the studies of the GluN2A- and GluN2B-containing NMDARs (Karakas and Furukawa, 2014; Lee et al., 2014; Lu et al., 2017) to facilitate expression, purification, and structural analysis (Figure S1A–C). The resulting construct, $GluN2C_{EM}$, together with GluN1a, forms the channel with functional properties intrinsic to the wildtype GluN2C, which include higher efficacy of D-cycloserine (DCS) over glycine and potentiation by the GluN2C-specific PAM, PYD-106 (Khatri et al., 2014) (Figure S1D–J). The $GluN2C_{EM}$ slowly desensitize upon agonist application, unlike the wildtype, implying a potential functional role of CTD as shown in other NMDAR subtypes (Choi et al., 2013). The modified construct was expressed in the EarlyBac insect expression system (Furukawa et al., 2021) and purified to homogeneity for structural analysis (Figure S1; Methods S1).

The structure was first obtained in the presence of DCS and glutamate to capture the full-agonist-bound state (Figure 1; Data S1). The single-particle cryo-EM analysis resulted in the two three-dimensional (3D) classes, which we named ‘intact’ (Figure 1A) and ‘splayed’ (Figure 1B) at 3.7 and 3.8 Å overall resolutions, respectively (Figure S2A–S2B). The GluN2C subunit has the ATD, LBD, and TMD with similar patterns of secondary structures

to the previously studied GluN2A and GluN2B subunits (Figure 1). The ‘intact’ 3D class had well-resolved extracellular domains (ATDs and LBDs) but not TMDs (Figure 1A). Extensive focused 3D classification did not capture the TMD, indicating heterogeneous orientations between the extracellular domains and the TMD. In this 3D class, two copies of GluN1a and GluN2C subunits formed a dimer of GluN1a-2C heterodimers with the heterodimeric pairs swapped at the ATD and LBD layers (Figure 1C). This ‘staggered’ assembly pattern was also observed in the GluN2A- and GluN2B-containing NMDARs as well as in AMPAR and kainate receptors (Herguedas et al., 2016; Khanra et al., 2021; Meyerson et al., 2014; Sobolevsky et al., 2009), where the interactions between ATD and LBD are more extensive in the NMDARs than the non-NMDARs (Karakas et al., 2015; Regan et al., 2015; Wang and Furukawa, 2019). The ‘splayed’ 3D class had well-resolved cryo-EM density in the TMD, LBD, and one GluN1a-2C ATD heterodimer (Figure 1B). The other GluN1a and GluN2C ATDs are mobile and do not form a heterodimer as observed by focused 3D classification (Figure 1B, D; asterisks). At the LBD layer, one GluN1a-2C heterodimer is in a ‘back-to-back’ arrangement similar to the one observed in the ‘intact’ 3D class, and the subunit interface of the other GluN1a-2C LBD heterodimer is reoriented by rotation of GluN2C LBD by 83° (Figure 1D, LBD, arrow).

Overall, the tetrameric assembly of GluN1a-2C NMDAR is asymmetrical, unlike GluN1-2A and GluN1-2B NMDARs with C2 or pseudo-C2 symmetry at physiological pH in the absence of zinc (Chou et al., 2020; Jalali-Yazdi et al., 2018; Karakas and Furukawa, 2014; Tajima et al., 2016; Zhang et al., 2018). In the ‘intact’ 3D class, no symmetry is observed at the ATD layer, whereas two pairs of GluN1a-2C LBD heterodimers are related by C2 symmetry (Figure 1C). In the ‘splayed’ 3D class, no symmetry is observed in the entire extracellular region, whereas C2 symmetry is present around the channel gate formed by the M3 helices in the TMD (Figure 1D). The subunit rupturing of the ‘splayed’ 3D class is reminiscent of that observed in the inhibited state of GluN1-2A NMDAR at high Zn^{2+} concentration and low pH (Jalali-Yazdi et al., 2018). The overall conformation of the ‘intact’ 3D class is similar to the active conformation of GluN1b-2B NMDARs, which has been suggested to represent the non-desensitizing partially open state (Chou et al., 2020; Tajima et al., 2016; Tajima et al., 2022). In this protein conformation, the dimer-of-dimers arrangement of GluN1-2C LBDs are oriented to pull the LBD-TMD linkers apart (64.5 Å) compared to the non-active conformation of the GluN1b-2B NMDAR (50.3 Å), which creates the tension that drives channel gating (Figure 1E). The equivalent distance in the ‘splayed’ 3D class of the GluN1a-2C NMDAR is short at 44.8 Å, where the linker tension is insufficient for channel gating (Figure 1F), indicating that the ‘splayed’ 3D class likely represents an inactive state.

The physiological relevance of the observed subunit arrangement was validated by the formation of inter-subunit disulfide bonds by site-directed incorporation of cysteines at the GluN1a-GluN2C subunit interface (Figure S3A–S3B). Also, both ‘intact’ and ‘splayed’ 3D classes were observed in the GluN1a-2C NMDAR sample prepared in lipidic nanodiscs (Figure S4A–S4B; Methods S2), representing the more native-like condition. Furthermore, we validated the existence of the ‘splayed’ 3D class in the purified sample. For this, we mutated the residue, GluN2C-Thr756, buried in the GluN1a-2C LBD dimer in the ‘intact’ 3D class but exposed in the ‘splayed’ 3D class, to cysteine (Figure S3C). We observed that

this cysteine mutant is solvent accessible and can be labeled with FITC-maleimide while no labeling was observed in the wildtype channel (Figure S3D). Importantly, modification of GluN2C-Thr756Cys with 2-(trimethylammonium)ethyl methanethiosulfonate (MTSET), which prevents the 'splayed' 3D class from transitioning to the 'intact' 3D class, reduces the macroscopic current as assessed by TEVC (Figure S3E), indicating that the 'splayed' conformer likely represents an inhibited state.

Comparison of domain architectures between GluN2C and GluN2A/2B

The current study provides the experimentally determined structure of GluN2C and thus, permits a detailed comparison with the available structures of the GluN2A and GluN2B subunits at ATDs, LBDs, and TMDs. The overall architectures of LBDs are similar, where the glutamate-bound GluN2C LBD has the similar extent of the D1-D2 bi-lobe closure to that in the glutamate-bound GluN2A or GluN2B LBDs (Figure 2A; left). Furthermore, the heterodimeric arrangement of the GluN1a-2C LBDs in the 'intact' 3D class is similar to those in the GluN1-2A and GluN1-2B NMDARs (Figure 2A; right). ATD is the major determinant of the subtype-specific functions, including open probability and deactivation speeds (Gielen et al., 2009; Yuan et al., 2009) and compound binding for allosteric modulation (Furukawa, 2012; Regan et al., 2015; Wang and Furukawa, 2019). In our agonist-bound structures, the GluN2C ATDs have the bi-lobed architecture composed of R1 and R2 domains in an open conformation (Figure 2C). It has been known that the closure and opening of the GluN2A and GluN2B ATD bi-lobes lead to inhibition and activation, respectively (Chou et al., 2020; Jalali-Yazdi et al., 2018; Tajima et al., 2016; Zhang et al., 2018). For example, the bi-lobes are open at high pH whereas they are closed in inhibitory conditions including low pH (GluN2A and 2B) (Zhang et al., 2018), in the presence of zinc (GluN2A and 2B) (Jalali-Yazdi et al., 2018; Karakas et al., 2009; Romero-Hernandez et al., 2016), or in the presence of a negative allosteric inhibitor, such as ifenprodil (GluN2B) (Karakas et al., 2011; Regan et al., 2019; Stroebel et al., 2016) (Hansen et al., 2021). Our GluN1a-2C NMDAR structure harbors the GluN2C ATD bi-lobe in the open conformation due to the lack of residues that mediate favorable R1-R2 interactions, unlike GluN2A and GluN2B (Figure 2C), which may contribute to lower pH sensitivity compared to GluN2A, GluN2B, and GluN2D (Traynelis et al., 1995). Furthermore, the GluN2C ATD bi-lobe does not contain any coordinating residues for Zn^{2+} such as aspartate, glutamate, and histidine at the R1-R2 interface, unlike GluN2A and GluN2B ATDs (Figure 2C), consistent with the lack of ATD-mediated Zn^{2+}inhibition in the GluN1-2C NMDAR (Traynelis et al., 1995). Furthermore, the GluN1-2C subunit interface at ATD is similar to the GluN1-2B ATD interface in the active conformation (Chou et al., 2020; Tajima et al., 2016) where GluN2B ATD bi-lobe is open and negative allosteric modulator (NAM) binding pocket at the subunit interface is collapsed with a minimal solvent accessible volume consistent with no binding of similar allosteric modulators in the GluN1-2C NMDAR ATD (Figure 2D).

The GluN1a-2C TMD has similar features to those of GluN1-2A or GluN1-2B NMDARs. The TMD in the 'splayed' 3D class has highly ordered cryo-EM density especially around the pore formed by the M3 helices (Figure 1B and S2D). The TMD architecture and the tetrameric arrangement are similar to GluN1-2A and GluN1-2B NMDARs where the channel gate is formed by the M3 helices, the channel pore by the P-loop containing the

M2 helix, and the M1 and M4 helices surround the central channel to mediate further subunit interactions (Figure 2E–2F). The pore contains the Thr-, hydrophobic-, and Asn-rings, which are critical for the binding of channel blockers (Chou et al., 2022). Locally, the positions of the Asn-ring in GluN2C are closer to the intracellular side than that in GluN2B, whereas the Thr- and hydrophobic-rings residues are superimposable (Figure 2F; Superposition). The Asn-ring residues are known to be critical for voltage-dependent magnesium block (Chou et al., 2022; Kashiwagi et al., 2002), and the difference in the Asn residue orientations may partially account for the difference in magnesium coordination and sensitivity to magnesium channel block between GluN2A/2B and GluN2C/2D. Nevertheless, the overall structural similarities in the LBDs and TMDs between GluN1-2A, GluN1-2B, and GluN1-2C NMDARs are consistent with the view that these two domains mediate ligand-gated ion channel activity, whereas ATD modulates the activity in a subtype-specific manner (Furukawa, 2012; Hansen et al., 2021; Regan et al., 2015).

Conformational asymmetry within the GluN1a-2C NMDAR tetramer

The unique structural feature of GluN2C is the variability of inter ATD- LBD domain orientations characterized by ‘bent,’ ‘straight,’ and ‘broken’ (Figure 3A–3B). The ‘intact’ 3D class contains one ‘bent’-GluN2C and one ‘straight’-GluN2C (Figure 3A), whereas the ‘splayed’ 3D class has one ‘bent’-GluN2C and one ‘broken’-GluN2C (Figure 3B). While the ‘broken’ conformation is highly heterogeneous, the ‘bent’ and ‘straight’ conformations have the defined orientation between the ATDs and LBDs (Figure 3A–B). The two GluN1a-2C LBD dimers are arranged in a two-fold symmetrical manner, whereas the ATD dimers are not, showing the intrinsic symmetry mismatch between the ATD and LBD layers (Figure 3C).

In the ‘intact’ 3D class, the ‘bent’-GluN2C harbors a well-ordered linker motif between GluN2C ATD and LBD, which interacts with Asn-linked glycosylation from the adjacent GluN1a subunit at Asn368 (Figure 3C). No such interaction was observed in the ‘straight’-GluN2C. The ATD-LBD linkers in NMDARs have been shown to be critical for controlling subtype-specific functions, including open probability and deactivation speeds (Gielen et al., 2009; Yuan et al., 2009). To assess the functional importance of this unique interaction, we incorporated the GluN1a-Asn368Gln mutation to remove the Asn-linked glycosylation and estimated changes in channel open probability (Po) by measuring the onset speeds of MK801 block by the whole-cell patch-clamp electrophysiology. Our analysis showed that the onset of MK801 block is ~1.7-fold faster in the mutant than the wildtype indicating that removal of glycosylation at GluN1a-Asn368 resulted in higher Po (Figure 3D). Furthermore, this mutant displayed a decreased potentiation by PYD-106 (Figure 3E). Thus, the interaction between the GluN2C ATD-LBD linker and the Asn-linked glycosylation at GluN1a-Asn368, which is uniquely occurring in the ‘bent’ conformation, contributes to lowering Po, and increasing the sensitivity to PYD-106. Taken together, the asymmetric nature of the GluN1a-2C tetramer presents a means to tune the receptor function.

PYD-106 binds to the GluN2C ATD-LBD interface in ‘straight’ conformation

Specific potentiation of NMDARs containing GluN2C may be clinically advantageous since these receptors are discretely expressed in specific brain regions such as the cerebellum

where hypofunction is associated with schizophrenia (Belforte et al., 2010; Khlestova et al., 2016; Nakazawa and Sapkota, 2020). PYD-106 has been developed as a GluN2C-specific PAM; however, the structural insights into subtype-specific binding and potentiation have been limited. In order to rectify this shortfall, we conducted single-particle cryo-EM on the GluN1a-2C NMDARs in the presence of DCS, glutamate, and PYD-106 (Figure 4 and S2E–S2H; Table S1; Methods S1). As in the agonist-bound structure (Figure 1 and S2A), our single-particle analysis showed the 'intact' and 'splayed' 3D classes (Figure S2B). However, the ratio of the particle numbers between the 'intact' and 'splayed' conformations (intact/splayed) increased substantially from ~0.64 to ~1.57, implying that the binding of PYD-106 stabilizes the 'intact' 3D class (Figure S2). This observation, together with the MTSET modification experiment (Figure S3E and S2F), supports the view that 'intact' and 'splayed' 3D classes are in dynamic equilibrium. Our structural inspection detected the binding of one PYD-106 molecule on the 'straight'-GluN2C in the 'intact' 3D class (Figure 4A–4B). No binding was detected in the 'bent'-GluN2C or in any of the subunits in the 'splayed' 3D class. PYD-106 binds to the ATD-LBD interface and only locally alters the orientation of the binding residues compared to the agonist-bound structure (Figure 1A and 3A, RMSD = 0.984 over 597 residues in ATD and LBD). Most of the interacting residues in GluN2C ATD are not conserved among all the other GluN2 subunits. The binding pocket is formed by residues from the inter α4'-β6', α5'-β7', and α6'-β8' loops in the GluN2C ATD and around the B' helix in the GluN2C LBD (Figure 4B). Specific interactions include hydrophilic interactions between the pyrrole ring moiety and Arg194 and Arg467 and hydrophobic interactions between the indole ring moiety and Leu196 and Pro222. Furthermore, the pocket is surrounded by residues including Ser163, Asp220, and Tyr473 (Figure 4B). Such pocket does not exist in the 'bent' conformation since the ATD-LBD interface at this site is loose compared to the 'straight' conformation, as demonstrated by the distance difference between the alpha carbon of Asp220 and Lys470 (Figure 4C, dashed lines).

To validate the binding mode of PYD-106 observed in the present study, we conducted site-directed mutagenesis on directly interacting residues, Arg194, Leu196, Asp220, and Pro222, and assessed the PAM activity of PYD-106 by measuring macroscopic current using TEVC (Figure 4D). The single point mutations, Arg194Glu, Leu196Glu, Asp220His, and Pro222Gly resulted in a robust reduction of the PAM activity, whereas the mutation on the non-interacting Tyr473 (Tyr473Ala) did not have any effect. Most notably, the Pro222Gly mutation completely removes the PAM activity (Figure 4D). In contrast, the Ser163Tyr mutation, which was predicted to form an additional hydrophobic interaction with the benzoate group resulted in higher PAM activity (~3-fold potentiation) (Figure 4D).

To assess if PYD-106 exclusively binds to the 'straight' conformation, we stabilized the 'bent' conformation by engineering a disulfide bridge at the GluN2C ATD-LBD interface and assessed the PAM activity by TEVC. Specifically, we incorporated the mutations, Val379Cys and Gly424Cys in GluN2C ATD and LBD, respectively (Figure 4E–4F). Importantly, these sites are distant from the PYD-106 binding pocket therefore, the mutations themselves would not interfere with the PYD-106 binding directly. We assumed that this mutant receptor harbors two GluN2Cs in the 'bent' conformation (Figure 4E). The TEVC recording on the Val379Cys/Gly424Cys double mutant completely abolished the PAM activity of PYD-106 (Figure 4F). The PAM activity is recovered when the engineered

disulfide bond is disrupted by dithiothreitol (DTT). Consistently, the single-point mutants (Val379Cys or Gly424Cys), which do not form the disulfide bridge retain the PAM activity (Figure 4F). Furthermore, the application of DTT to the single-point mutants or the wildtype results in a decrease of their macroscopic currents, rather than an increase as observed in the double mutant. Thus, overall, the structural and electrophysiological experiments above supported the view that PYD-106 binds only to the 'straight' conformation but not the 'bent' conformation. Stabilizing the 'straight'-GluN2C by the PYD-106 binding at the ATD-LBD interface favors the GluN1a-2C tetrameric assembly in the more active 'intact' 3D class as the 'straight' conformation is unique to the 'intact' 3D class and not observed in the inhibitory 'splayed' 3D class. It is worth noting that this pocket does not exist in GluN1, GluN2A, and GluN2B subunits.

Cryo-EM structure of GluN1a-2A-2C NMDAR reveals 'intact' tetramer

It has been previously shown that predominant NMDARs in cerebellar granule cells in adult brains are tri-heteromeric receptors containing GluN1, GluN2A, and GluN2C subunits (Bhattacharya et al., 2018). The GluN1-2A-2C NMDAR has the intermediate deactivation speed between GluN1-2A and GluN1-2C and single-channel behavior, including bursts similar to GluN1-2A and open probability similar to GluN1-2C (Bhattacharya et al., 2018; Bhattacharya and Traynelis, 2018). To gain mechanistic insights into these unique functional properties, we sought to unravel patterns of subunit stoichiometry and arrangement by single-particle cryo-EM. Here, we co-expressed and purified GluN1a, GluN2C, and GluN2A, and bound an anti-GluN2A nanobody to facilitate the distinction between GluN2A and GluN2C in a single-particle analysis (see Methods; Methods S2). We obtained the agonists-bound (DCS/glutamate) GluN1a-2A-2C NMDAR structure at 4.2 Å and revealed the tetrameric arrangement of the GluN1a-2A-2C NMDAR, containing two GluN1a subunits, one GluN2A subunit, and one GluN2C subunit (Figure 5 and S4C–S4D; Table S1; Methods S2). Notably, there was only one major 3D class, which resembled the 'intact' 3D class in GluN1a-2C NMDAR (Figure 5A and 5B), where GluN2A had a conformation similar to the 'straight'-GluN2C and GluN2C was in the 'bent' conformation (Figure 5B), and there was no evidence for the existence of the 'splayed' 3D class. This indicated that incorporation of the GluN2A subunit favored the 'intact' 3D class and stabilized the active conformation, where gating ring residues were positioned to elicit tension to the LBD-TMD linkers to favor gating (Figure 5C) (Chou et al., 2020). As in the case of the 'intact' 3D class of GluN1a-2C NMDAR, the TMD region was not resolved in the GluN1a-2A-2C NMDAR. The absence of the 'straight' conformation of GluN2C in the GluN1a-2A-2C NMDAR was consistent with no effect of PYD-106 on this tri-heteromeric receptor (Khatri et al., 2014) as PYD-106 can only bind to the 'straight'-GluN2C (Figure 4). Furthermore, the conformation of the GluN2A subunit was distinct from those observed in GluN1-2A di-heteromeric and GluN1-2A-2B tri-heteromeric NMDARs (Figure S5) in that the ATD-LBD was more straightened (~127° in GluN1a-2A-2C, ~124° in GluN1a-2A-2B, and ~120° in GluN1a-2A; Figure 5B and S5). As in the 'intact' 3D class of the di-heteromeric GluN1a-2C NMDARs, the subunits in the LBD layer in GluN1a-2A-2C NMDARs were arranged in a pseudo-two-fold symmetry manner whereas the ATD layer had no symmetry (Figure 5D–5E) stemming from the different ATD-LBD orientations between GluN2A and GluN2C (Figure 5B). The inter-subunit and -domain interactions between GluN2A and GluN2C are

unique. While both the GluN2A and GluN2C interfaces involve GluN1a loop1 and GluN2 loop2 from LBD and the α5' loop from ATD, the GluN2C interface uniquely contains β15' in proximity (Figure 5F). The conservation of unique interactions to a similar extent may explain the intermediate functional characteristics of GluN1-2A-2C NMDAR pharmacology, time course, and channel activity. The extent of ATD-LBD interactions in GluN1a-2A-2B NMDAR was previously shown to be different, where GluN2A has more extensive ATD-LBD interactions than GluN2B, which was suggested to be consistent with the functional dominance of GluN2A over GluN2B (Lu et al., 2017).

Cryo-EM structure of GluN1a-2D NMDAR

The GluN2D subunit is more similar to GluN2C than GluN2A or 2B in terms of amino acid sequences even though there are a number of functional differences such as slow deactivation. To understand if GluN2D-containing NMDARs possess a similar subunit and domain arrangement to the GluN2C-containing NMDARs, we conducted single-particle cryo-EM on the CTD deleted GluN1a-2D NMDARs and obtained the structure at 3.4 Å overall resolution (Figure 6 and S6A–S6C; Methods S3). Our analysis revealed one 3D class that appeared similar to a conventional NMDAR channel with the dimer of heterodimeric arrangement like all the other NMDARs with ordered density for ATD, LBD, and TMD (Figure 6A–6B). The GluN1a-2D NMDAR tetramer has a pseudo-symmetrical subunit arrangement where two GluN2D subunits within the tetramer have similar ATD-LBD orientations (123° and 126°; Figure S5) like GluN1a-2A, GluN1-2B, or GluN1-2A-2B NMDARs but unlike the GluN1a-2C or GluN1a-2A-2C NMDARs (Figure S5). This observation indicates that the heterogeneity in the ATD-LBD orientation is a feature unique to the GluN2C-containing NMDARs. The architecture of the GluN2D LBD and the heterodimeric arrangement in the GluN1a-2D LBDs are similar to the GluN2A- or GluN2B-containing NMDARs (Figure 6C). The GluN2D ATD, like, GluN2C ATD, is in an open conformation, and lacks the Zn^{2+}-binding residues at the R1-R2 cleft (Figure 6D; left). The GluN1a-2D ATD heterodimeric interface has a minimal solvent accessible volume, which is consistent with no binding of ifenprodil-like NAM (Figure 6D; right). The GluN2D TMD is similar to all the other NMDARs where the channel gate is formed by the M3 helices and the M1 and M4 helices surround the central pore (Figure 6E–6F). The TMD pore contains the Thr-ring and the hydrophobic-ring formed by residues from the M3 helices like all the other NMDARs, whereas the Asn-ring was not clearly visible in our current structure likely stemming from the high mobility of the P-loop. Finally, the conformation of GluN1a-2D NMDAR is similar to the 'non-active2' in GluN1-2B NMDARs (Chou et al., 2020; Tajima et al., 2016) where the tension of the LBD-TMD linkers is insufficient for channel gating (Figure 6G). This is in contrast to GluN1a-2C or GluN1a-2A-2C NMDARs, which are stabilized in non-desensitized 'active' form (Figure 1E and 5C). Overall, the GluN2D-containing NMDAR has a pseudo-C2-symmetrical subunit arrangement, which is stabilized in the 'non-active' conformation, unlike the GluN2C-containing NMDARs. It is worth mentioning that our cryo-EM structure of GluN1a-2D NMDAR bound to glycine and glutamate contains GluN2D LBD with the 'hinge loop' conformation specifically observed for the crystal structure of the L-glutamate-bound GluN2D LBD (Figure S6D). Our current structure corroborates the previous finding that the slow deactivation of GluN1a-2D

NMDARs is unique to glutamate but not other agonists such as NMDA, which may be caused by the unique ‘hinge loop’ conformation elicited by glutamate (Vance et al., 2011).

Discussion

Our current work provides the structure of the GluN2C- and GluN2D-containing NMDARs. They have discrete patterns of expression in brain regions and distinct properties, which are crucial for fundamental brain functions and development. Insights gained in this study provide the field with the blueprint to study the structure, function, and pharmacological specificity of the GluN1a-2C di-heteromeric, GluN1a-2A-2C tri-heteromeric, and GluN1a-2D di-heteromeric NMDARs. Our major finding is that the tetrameric assembly of the GluN2C-containing NMDAR is more asymmetric than any other GluN1-2 NMDARs. The asymmetry of the GluN2C-containing NMDARs stems from the existence of the three distinct conformations, ‘straight’, ‘bent’, and ‘broken’ in the extracellular region of GluN2C (Figure 7).’ Together with GluN1, they form two kinds of tetramers, the ‘intact’ and ‘splayed’ 3D classes, harboring straight/bent and bent/broken conformer combinations, respectively (Figure 7). The ‘splayed’ conformation was validated by the accessibility of GluN2C-Thr756Cys, which is exposed in the ‘splayed’ but buried in a subunit interface in the ‘intact,’ to FITC-maleimide (Figure S3C–S3D). The channel activity attenuation, electrophysiologically observed by the stabilization of the ‘splayed’ conformation (by the MTSET modification of GluN2C-Thr756Cys), indicates that the ‘splayed’ conformation likely represents an inhibited state (Figure S3E). These observations support the view that the ‘splayed’ conformation is physiological and is not caused by experimental artifacts such as a water-air interface potentially introduced during a cryo-EM grid preparation.

The unique domain orientation in the GluN2C subunit defines the subtype-specific features, including binding of PYD-106 and functional tuning by Asn-linked glycosylation. The GluN2C PAM, PYD-106, selectively binds to the ATD-LBD interface of the ‘straight’ conformation and locks it, thereby stabilizing the more active ‘intact’ 3D class (Figure 7). The ‘straight’-GluN2C is replaced by the GluN2A subunit in the similar ATD-LBD arrangement, and consequently, the GluN1-2A-2C NMDAR has a similar subunit arrangement to the ‘intact’ GluN1a-2C NMDARs. Indeed, no ‘splayed’ 3D class was observed in the GluN1a-2A-2C NMDARs indicating why the GluN1a-2A-2C NMDAR may have a higher Po and open duration compared to the GluN1a-2C NMDAR (Bhattacharya et al., 2018). During the early brain development, we speculate that GluN1-2C NMDARs may form in some cells, but the GluN2C subunit in the ‘straight’ conformation may be gradually replaced by the GluN2A subunit to form the tri-heteromeric GluN1-2A-2C NMDARs later. The Asn-linked glycosylation at GluN1a-Asn368 and the ATD-LBD linker of the ‘bent’-GluN2C reduces the Po moderately (Figure 3D). The ATD-LBD linker is known as an important determinant for subtype-selective channel activity (Gielen et al., 2009; Yuan et al., 2009) and was shown previously to interact with the motif that is encoded by exon5 (exon5-motif) in the GluN1b splice variant (Regan et al., 2018).

Finally, the subunit arrangement of the GluN1a-2D NMDAR is pseudo-two-fold symmetrical like GluN1a-2A or GluN1a-2B NMDARs and is not similar to the GluN2C-

containing NMDARs even though GluN2D has higher sequence identity with GluN2C than GluN2A or 2B. This demonstrates that the asymmetrical nature of GluN2C is unique among the GluN2-containing NMDARs. Furthermore, our glutamate-bound GluN1a-2D NMDAR structure has the 'hinge' conformation unique to the binding of glutamate, but not other agonists as previously shown by a series of GluN2D LBD crystal structures (Figure S6D) (Vance et al., 2011). However, the precise mechanism underlying the glutamate-specific slow deactivation in GluN2D in the context of the intact NMDAR remains an open question and may require more structural data. Overall, this study revealed the structural diversity of NMDAR subtypes, where the GluN2C-containing NMDARs show conformation and subunit arrangement, highly distinct from GluN1-2A, GluN1-2B, GluN1-2A-2B, and GluN1-2D NMDARs. These conformational diversities of NMDAR subunits likely account for highly diverse functional properties of the NMDAR subtypes.

Limitations of the study

Our work provides the structural framework to study GluN1a-2C, GluN1a-2D, and GluN1a-2A-2C NMDARs. It also reveals the binding site of the GluN2C PAM, PYD-106. Nevertheless, the techniques and approaches implemented here have some limitations. Structures presented here were determined from samples solubilized in detergent (and reconstituted into lipid nanodisc in one case) and purified from a heterologous expression system. Therefore, the 'splayed' and 'intact' conformations observed in this study may not represent the full range of conformational states that might have been captured in a more native membrane environment. Isolation of the NMDARs from animal brains may answer some lipid-related questions. Furthermore, in this study, we removed CTDs from the GluN2A, GluN2C, and GluN2D subunits as in all other previous studies to permit recombinant expression and purification of the NMDAR proteins for structural analyses. Therefore, questions related to the role of CTDs in the downstream signal transduction or channel function regulations cannot be answered by the current study. CTDs from GluN2s are predicted to be disordered; therefore, identifying interacting proteins and mapping the interactome around CTDs by a proteomics approach may partly fulfill this shortfall.

STAR Methods

RESOURCE AVAILABILITY

Lead contact—Further information and requests for resources and reagents should be directed to the Lead Contact, Hiro Furukawa (furukawa@cshl.edu).

Materials Availability—All unique reagents generated in this study are available from the Lead Contact with a completed Materials Transfer Agreement.

Data and Code Availability

- Atomic model coordinates and cryo-EM maps have been deposited in the RCSB and EMDB, respectively, under the accession codes (PDBID: 8E92, 8E93, 8E94, 8E96, 8E97, 8E98, 8E99, and EMDBID: EMD-27953, EMD-27954,

EMD-27955, EMD-27957, EMD-27958, EMD-27959, EMD-27960, EMD-27961, EMD-28051, EMD-28052, EMD-28053).

- No original code is written and used in this paper.
- Any additional information required to reprocess and reanalyze the reported data in this paper is available from the lead contact upon request.

EXPERIMENTAL MODEL AND SUBJECT DETAILS

*Sf*9 cells were cultured in HyClone CCM3 cell culture medium (GE Healthcare) at 27°. *Xenopus laevis* oocytes used in electrophysiology experiments were cultured in 0.5X HyClone Leibovitz L-15 Medium at 18°C. HEK293 cells used in electrophysiology experiments were cultured in DMEM cell culture medium (GIBCO) supplemented with 10% fetal bovine serum at 37°C and 5% CO_2 (Sigma-Aldrich).

METHOD DETAILS

Protein expression and purification—The gene encoded human GluN1a (residues 19–847) and human GluN2C (residues 27–849) or human GluN2D (residues 28–879) were cloned into the EarlyBac vectors, pUCDMp10 and pFp10, respectively (Furukawa et al., 2021). The signal peptide from *Xenopus laevis* GluN1 was fused to the N-terminus of GluN2C or GluN2D followed by a dual strep-tag and a thrombin cleavage site. To promote protein stability and expression, a cysteine at the N-terminal of GluN1a was mutated to serine (Cys22Ser) and the ER retention signal (RRK) at the end of the GluN1a construct was removed by the mutations, Arg844Gln, Arg845Gly, and Lys846Ala. For the human tri-heteromeric GluN1a-2A-2C NMDAR, we tethered the GluN2C construct above and the GluN2A construct with the 2A self-cleaving peptide (P2A: ATNFSLLKQAGDVEENPGP) in pFp10. The GluN2A construct contained residues 29–851 fused to the *Xenopus laevis* GluN1 signal peptide and the 1D4 epitope (TETSQVAPA) at N- and C-terminus, respectively. In addition, three cysteines were mutated to serines (Cys399Ser, Cys460Ser, and Cys848Ser) for protein stability. For expression of both GluN1a-2C and GluN1a-2A-2C NMDARs, pFp10 (GluN2s) were tethered with pUCDMp10 (GluN1a) by Cre-lox recombination for production of baculoviruses harboring all subunit genes.

The human GluN1a-2C or GluN1a-2D NMDAR receptors were expressed and purified by the purification protocol published previously (Furukawa et al., 2021). In brief, the *Sf*9 insect cells were infected by the baculovirus at a cell density of 4×10^6 cells/ml. The cells were harvested at 48 hours post-infection, resuspended in the purification buffer (20 mM HEPES-Na pH 7.5, 150 mM NaCl, 1 mM D-cycloserine or 1 mM glycine, 1 mM Na-Glutamate) supplemented with 1 mM phenylmethylsulphonyl fluoride (PMSF), and lysed by the high-pressure cell homogenizer (EmulsiFlex-C5, Avestin). The cell debris was removed by centrifugation at 5,000*g* and the membrane fraction was collected by ultracentrifugation (40k rpm at 4°C) of the supernatant. The pelleted membrane was then solubilized by 0.5% LMNG in the purification buffer with gentle stirring for 2 hours at 4°C followed by ultracentrifugation. The supernatant was subjected to Strep-Tactin Sepharose by gravity flow followed by washes with the purification buffer and the purification

buffer with 3 mM Mg-ATP. The protein was eluted by the purification buffer with 3 mM desthiobiotin in the purification buffer. The eluted proteins were subjected to size-exclusion chromatography (SEC). For the GluN1a-2A-2C NMDAR, the protein was further purified using 1D4-antibody Sepharose after the Strep-Tactin chromatography step above. The column was washed with the purification buffer containing 0.3 mg/ml of GluN2A specific nanobody, Nb-4. The flow was stopped for 30 min to maximize the nanobody binding. The excessive Nb-4 was washed away by the purification buffer. The GluN1a-2A-2C-Nb-4 complex was eluted by 0.2 mg/ml 1D4 peptide.

Single-particle cryo-EM—The purified and concentrated (3mg/ml) proteins were vitrified on the glow-discharged UltrAufoil holey gold film grids (Quantifoil). Glow discharge took place in PELCO easiGlowTM glow discharge cleaning system (Ted Pella) for 25 sec under 15 mA. The grids were blotted at 4°C with 85% humidity with blot time of 2 sec under level 7 blot force. All the electron micrographs were acquired by Titan Krios (FEI) operating at 300 kV in couple with GIF quantum energy filter (Gatan Inc.) under 105k magnification. Micrographs were recorded as dose-fractionated movie frames by K3 direct electron detector (Gatan Inc.) in electron counting mode. The defocus was set with a range from −1.4 to −2.8 μm. The semi-automated data acquisition was executed by EPU. Micrographs were taken at 105k magnification. The images were fractionated into 30 frames between 0.06–0.07 seconds of exposure. Total exposure times between 1.8–2.1 seconds were accumulated under the electron flux of 1.80–1.92 $e^{-}/Å^2$/frame, yielding total doses between 54–57.6 $e^{-}/Å^2$ on the specimens. The movie alignment, CTF estimation, and particle picking were done using the program WARP (Tegunov and Cramer, 2019). The picked particle images were imported into the program cryoSPARC to perform 2D classification. *Ab-initio* 3D map generation, 3D refinement, 3D classification, Bayesian polishing, and per particle CTF refinement were done using the program RELION3.1 (Zivanov et al., 2019). The final 3D refinement and B-factor sharpening were done using the program cisTEM (Grant et al., 2018). Model fitting and building were done using UCSF Chimera (Pettersen et al., 2004) and COOT (Emsley et al., 2010). The final models were refined against the cryo-EM maps using Phenix real-space refinement (Adams et al., 2010) with secondary structure and Ramachandran restraints. The FSCs were calculated by phenix.mtriage. Summary of data collection and refinement statistics are shown in Table S1. The presentations of the structures were illustrated by the program PyMOL (Schrödinger, LLC.).

Two-electrode voltage clamp—cRNAs encoding human GluN1-4a and human GluN2C were injected into defolliculated *Xenopus laevis* oocytes (Ecocyte Bioscience) at 1:1 ratio (total of 6 – 25 ng). The oocytes were then incubated in the recovery medium (0.5X L-15 medium (Hyclone) buffered by 15 mM Na-HEPES at a final pH of 7.4), supplemented with 100 μg/ml streptomycin, and 100 U/ml penicillin at 18°C. Two-electrode voltage clamp (TEVC; Axoclamp-2B) recordings were performed between 24 to 48 hours after injection using an extracellular solution containing 5 mM HEPES, 100 mM NaCl, 0.3 mM $BaCl_2$, 10 mM Tricine at final pH 7.4 (adjusted with KOH). The current was measured using agarose-tipped microelectrode (0.4–0.9 MΩ) at the holding potential of −60 mV. Maximal response currents were evoked by 100 μM of D-cycloserine and 100 μM of L-glutamate. Data was acquired by the program PatchMaster (HEKA) and analyzed by Origin 8 (OriginLab Corp).

Patch-clamp electrophysiology—Human embryonic kidney (HEK 293) cells (ATCC CRL-1573; Manassas, VA, USA) were plated onto glass coverslips pre-treated with 0.1 mg/ml poly-D-lysine and maintained in DMEM/GlutaMax medium (GIBCO, 15140–122) supplemented with 10% fetal bovine serum and 10 U/ml penicillin and 10 μg/ml streptomycin at 37°C in a humidified atmosphere with 5% CO_2. The HEK cells were transiently transfected with plasmid cDNAs encoding WT or mutant human GluN1 plus rat GluN2C subunits along with GFP at a cDNA ratio of 1:1:1 (0.4 μg/μL) by using the calcium phosphate precipitation method (Yuan et al., 2009). After eight hours following the transfection, the media was replaced with DMEM/GlutaMax. 24–48 hours later, the cells on cover slips were moved to a submerged recording chamber with continuous perfusion with external recording solution that contained (in mM) 3 KCl, 150 NaCl, 1 $CaCl_2$, 10 HEPES, and 11 D-mannitol, with the pH adjusted to 7.4 by NaOH. External solution was filtered through 0.45 μm nylon filters under vacuum. The whole-cell voltage-clamp current recordings were performed with fire polished recording electrodes with a resistance of 3–4 MΩ that were made from thin-walled filamented borosilicate glass capillary tubes (TW150F-4, World Precision Instruments, Sarasota, FL, USA) filled with the internal pipette solution that contained (in mM) 110 D-gluconic acid, 110 CsOH, 30 CsCl, 5 HEPES, 4 NaCl, 0.5 $CaCl_2$, 2 $MgCl_2$, 5 BAPTA, 2 Na_2ATP, 0.3 Na_2GTP (pH was adjusted to 7.4 with CsOH; the osmolality was adjusted to 300–310 mOsmol/kg, 23°C using CsCl or water). The whole cell current responses were evoked by the application of maximally-effective concentrations of agonists (1 mM glutamate plus 0.1 mM glycine) at −60 mV holding potential (V_{HOLD}) and were recorded at room temperature (23°C) by a Warner 505B patch-clamp amplifier (Warner Instrument, Holliston MA, USA). After 2 sec application of glutamate and glycine, the solution was rapidly switched by a piezoelectric translator to one containing glutamate and glycine supplemented with 5 μM (+)MK-801. The current responses were filtered at 8 kHz (−3 dB, 8 pole Bessel, Frequency Devices, IL, USA) and digitized at 20 kHz using Digidata 1440A acquisition system (Molecular Devices, CA, USA) controlled by Clampex 10.3 (Molecular Devices, CA, USA). Traces were analyzed using ChannelLab software with one or two exponential fits to determine the time course for the onset of MK-801 block, according to the equation

$$Response = AmplitudeFAST(exp(-time/tauFAST)) + AmplitudeSLOW(exp(-time/tauSLOW))$$

where *tau* and *Amplitude* are the time constants and respective amplitude for the two components. The weighted time constant was calculated according to

$$tauWEIGHTED = (AmplitudeFAST\,tauFAST + AmplitudeSLOW\,tauSLOW) / (AmplitudeFAST + AmplitudeSLOW)$$

QUANTIFICATION AND STATISTICAL ANLYSIS

Data processing and statistical analysis of electrophysiology data were conducted using the software Origin and Prism. The unpaired Student's t-test was implemented for analyses and comparison of all site-directed mutants. The n values in these experiments represent the numbers of *Xenopus* oocytes or HEK293 cells from which electrophysiological experiments were conducted. The data points are represented as mean ± SD. The information above is

described in the figure legend of Figures 4, S1, and S3. No method was applied to determine whether the data met the assumptions of the statistical approach. The resolution of the cryo-EM maps was estimated by the FSC = 0.143 criteria, calculated from two half maps with a soft mask. Details of data processing statistics and map quantifications are listed in Table S1.

Supplementary Material

Refer to Web version on PubMed Central for supplementary material.

Acknowledgments

We thank D. Thomas and M. Wang for managing the cryo-EM facility and the computing facility at Cold Spring Harbor Laboratory, respectively. K. Michalski isolated the anti-GluN2A nanobody. We thank C. Camp amd R. Perszyk for sharing unpublished data, and J. Allen, S. Kim, and J. Zhang for excellent technical assistance. This work was supported by NIH NS11745 and 113632 (HF), MH085926 (HF), NS111619 (SFT), Austin's purpose (HF and SFT), Robertson funds at Cold Spring Harbor Laboratory, Doug Fox Alzheimer's fund, Heartfelt Wing Alzheimer's fund, and the Gertrude and Louis Feil Family Trust (to HF).

Declaration of Interests

S.T. is PI on a research grant from Janssen to Emory University School of Medicine, is a member of the Scientific Advisory Board for Sage Therapeutics, Eumentis Therapeutics, and CombinedBrain, is a senior advisor for GRIN Therapeutics, is on the Medical Advisory Board for the CureGRIN Foundation and the GRIN2B Foundation, is co-founder of NeurOp Inc and Agrithera, is on the Board of Directors for NeurOp Inc, and is co-inventor on Emory-owned Intellectual Property that includes allosteric modulators of NMDAR function. The other authors declare no competing interests.

References

Adams PD, Afonine PV, Bunkoczi G, Chen VB, Davis IW, Echols N, Headd JJ, Hung LW, Kapral GJ, Grosse-Kunstleve RW, et al. (2010). PHENIX: a comprehensive Python-based system for macromolecular structure solution. Acta Crystallogr D Biol Crystallogr 66, 213–221 10.1107/S0907444909052925 [PubMed: 20124702]

Akazawa C, Shigemoto R, Bessho Y, Nakanishi S, and Mizuno N (1994). Differential expression of five N-methyl-D-aspartate receptor subunit mRNAs in the cerebellum of developing and adult rats. Journal of Comparative Neurology 347, 150–160 http://doi.org/10.1002/cne.903470112 [PubMed: 7798379]

Allgaier C, Durmaz M, Müller D, Franke H, Poelchen W, Wirkner K, and Illes P (2001). Single-cell RT-PCR analysis of N-methyl-D-aspartate receptor subunit expression in rat locus coeruleus neurones. Naunyn-Schmiedeberg's Archives of Pharmacology 363, 120–123 10.1007/s002100000348 [PubMed: 11191830]

Belforte JE, Zsiros V, Sklar ER, Jiang Z, Yu G, Li Y, Quinlan EM, and Nakazawa K (2010). Postnatal NMDA receptor ablation in corticolimbic interneurons confers schizophrenia-like phenotypes. Nature Neuroscience 13, 76–83 10.1038/nn.2447 [PubMed: 19915563]

Bhattacharya S, Khatri A, Swanger SA, DiRaddo JO, Yi F, Hansen KB, Yuan H, and Traynelis SF (2018). Triheteromeric GluN1/GluN2A/GluN2C NMDARs with Unique Single-Channel Properties Are the Dominant Receptor Population in Cerebellar Granule Cells. Neuron 99, 315–328 e315 10.1016/j.neuron.2018.06.010 [PubMed: 30056832]

Bhattacharya S, and Traynelis SF (2018). Unique Biology and Single-Channel Properties of GluN2A- and GluN2C-Containing Triheteromeric N-Methyl-D-Aspartate Receptors. J Exp Neurosci 12, 1179069518810423 10.1177/1179069518810423

Choi UB, Kazi R, Stenzoski N, Wollmuth LP, Uversky VN, and Bowen ME (2013). Modulating the intrinsic disorder in the cytoplasmic domain alters the biological activity of the N-methyl-

D-aspartate-sensitive glutamate receptor. The Journal of biological chemistry 288, 22506–22515 10.1074/jbc.M113.477810 [PubMed: 23782697]

Chou TH, Epstein M, Michalski K, Fine E, Biggin PC, and Furukawa H (2022). Structural insights into binding of therapeutic channel blockers in NMDA receptors. Nat Struct Mol Biol 29, 507–518 10.1038/s41594-022-00772-0 [PubMed: 35637422]

Chou TH, Tajima N, Romero-Hernandez A, and Furukawa H (2020). Structural Basis of Functional Transitions in Mammalian NMDA Receptors. Cell 182, 357–371 e313 10.1016/j.cell.2020.05.052 [PubMed: 32610085]

Cull-Candy SG, and Leszkiewicz DN (2004). Role of distinct NMDA receptor subtypes at central synapses. Sci STKE 2004, re16 10.1126/stke.2552004re16 [PubMed: 15494561]

Dravid SM, Prakash A, and Traynelis SF (2008). Activation of recombinant NR1/NR2C NMDA receptors. J Physiol 586, 4425–4439 10.1113/jphysiol.2008.158634 [PubMed: 18635641]

Emsley P, Lohkamp B, Scott WG, and Cowtan K (2010). Features and development of Coot. Acta Crystallogr D Biol Crystallogr 66, 486–501 10.1107/S0907444910007493 [PubMed: 20383002]

Furukawa H (2012). Structure and function of glutamate receptor amino terminal domains. J Physiol 590, 63–72 10.1113/jphysiol.2011.213850 [PubMed: 22106178]

Furukawa H, Simorowski N, and Michalski K (2021). Effective production of oligomeric membrane proteins by EarlyBac-insect cell system. Methods Enzymol 653, 3–19 10.1016/bs.mie.2020.12.019 [PubMed: 34099177]

Gielen M, Siegler Retchless B, Mony L, Johnson JW, and Paoletti P (2009). Mechanism of differential control of NMDA receptor activity by NR2 subunits. Nature 459, 703–707 10.1038/nature07993 [PubMed: 19404260]

Grant T, Rohou A, and Grigorieff N (2018). cisTEM, user-friendly software for single-particle image processing. Elife 7, e35383 10.7554/eLife.35383 [PubMed: 29513216]

Hansen KB, Tajima N, Risgaard R, Perszyk RE, Jorgensen L, Vance KM, Ogden KK, Clausen RP, Furukawa H, and Traynelis SF (2013). Structural determinants of agonist efficacy at the glutamate binding site of N-methyl-D-aspartate receptors. Molecular pharmacology 84, 114–127 10.1124/mol.113.085803 [PubMed: 23625947]

Hansen KB, Wollmuth LP, Bowie D, Furukawa H, Menniti FS, Sobolevsky AI, Swanson GT, Swanger SA, Greger IH, Nakagawa T, et al. (2021). Structure, Function, and Pharmacology of Glutamate Receptor Ion Channels. Pharmacol Rev 73, 298–487 10.1124/pharmrev.120.000131 [PubMed: 34753794]

Hansen KB, Yi F, Perszyk RE, Furukawa H, Wollmuth LP, Gibb AJ, and Traynelis SF (2018). Structure, function, and allosteric modulation of NMDA receptors. J Gen Physiol 150, 1081–1105 10.1085/jgp.201812032 [PubMed: 30037851]

Herguedas B, Garcia-Nafria J, Cais O, Fernandez-Leiro R, Krieger J, Ho H, and Greger IH (2016). Structure and organization of heteromeric AMPA-type glutamate receptors. Science 352, aad3873 10.1126/science.aad3873 [PubMed: 26966189]

Jalali-Yazdi F, Chowdhury S, Yoshioka C, and Gouaux E (2018). Mechanisms for Zinc and Proton Inhibition of the GluN1/GluN2A NMDA Receptor. Cell 175, 1520–1532 e1515 10.1016/j.cell.2018.10.043 [PubMed: 30500536]

Karakas E, and Furukawa H (2014). Crystal structure of a heterotetrameric NMDA receptor ion channel. Science 344, 992–997 10.1126/science.1251915 [PubMed: 24876489]

Karakas E, Regan MC, and Furukawa H (2015). Emerging structural insights into the function of ionotropic glutamate receptors. Trends in biochemical sciences 40, 328–337 10.1016/j.tibs.2015.04.002 [PubMed: 25941168]

Karakas E, Simorowski N, and Furukawa H (2009). Structure of the zinc-bound amino-terminal domain of the NMDA receptor NR2B subunit. The EMBO journal 28, 3910–3920 10.1038/emboj.2009.338 [PubMed: 19910922]

Karakas E, Simorowski N, and Furukawa H (2011). Subunit arrangement and phenylethanolamine binding in GluN1/GluN2B NMDA receptors. Nature 475, 249–253 10.1038/nature10180 [PubMed: 21677647]

Kashiwagi K, Masuko T, Nguyen CD, Kuno T, Tanaka I, Igarashi K, and Williams K (2002). Channel blockers acting at N-methyl-D-aspartate receptors: differential effects of mutations in the vestibule and ion channel pore. Mol Pharmacol 61, 533–545 10.1124/mol.61.3.533 [PubMed: 11854433]

Khanra N, Brown PM, Perozzo AM, Bowie D, and Meyerson JR (2021). Architecture and structural dynamics of the heteromeric GluK2/K5 kainate receptor. Elife 10 10.7554/eLife.66097

Khatri A, Burger PB, Swanger SA, Hansen KB, Zimmerman S, Karakas E, Liotta DC, Furukawa H, Snyder JP, and Traynelis SF (2014). Structural determinants and mechanism of action of a GluN2C-selective NMDA receptor positive allosteric modulator. Molecular pharmacology 86, 548–560 10.1124/mol.114.094516 [PubMed: 25205677]

Khlestova E, Johnson JW, Krystal JH, and Lisman J (2016). The Role of GluN2C-Containing NMDA Receptors in Ketamine's Psychotogenic Action and in Schizophrenia Models. The Journal of Neuroscience 36, 11151 10.1523/JNEUROSCI.1203-16.2016 [PubMed: 27807157]

Korotkova T, Fuchs EC, Ponomarenko A, von Engelhardt J, and Monyer H (2010). NMDA Receptor Ablation on Parvalbumin-Positive Interneurons Impairs Hippocampal Synchrony, Spatial Representations, and Working Memory. Neuron 68, 557–569 http://doi.org/10.1016/j.neuron.2010.09.017 [PubMed: 21040854]

Lee CH, Lu W, Michel JC, Goehring A, Du J, Song X, and Gouaux E (2014). NMDA receptor structures reveal subunit arrangement and pore architecture. Nature 511, 191–197 10.1038/nature13548 [PubMed: 25008524]

Lu C, Fu Z, Karavanov I, Yasuda RP, Wolfe BB, Buonanno A, and Vicini S (2006). NMDA Receptor Subtypes at Autaptic Synapses of Cerebellar Granule Neurons. Journal of Neurophysiology 96, 2282–2294 10.1152/jn.00078.2006 [PubMed: 16885526]

Lu W, Du J, Goehring A, and Gouaux E (2017). Cryo-EM structures of the triheteromeric NMDA receptor and its allosteric modulation. Science 355 10.1126/science.aal3729

Meyerson JR, Kumar J, Chittori S, Rao P, Pierson J, Bartesaghi A, Mayer ML, and Subramaniam S (2014). Structural mechanism of glutamate receptor activation and desensitization. Nature 514, 328–334 10.1038/nature13603 [PubMed: 25119039]

Monyer H, Burnashev N, Laurie DJ, Sakmann B, and Seeburg PH (1994). Developmental and regional expression in the rat brain and functional properties of four NMDA receptors. Neuron 12, 529–540 10.1016/0896-6273(94)90210-0 [PubMed: 7512349]

Nakazawa K, and Sapkota K (2020). The origin of NMDA receptor hypofunction in schizophrenia. Pharmacology & Therapeutics 205, 107426 http://doi.org/10.1016/j.pharmthera.2019.107426 [PubMed: 31629007]

Paoletti P, Bellone C, and Zhou Q (2013). NMDA receptor subunit diversity: impact on receptor properties, synaptic plasticity and disease. Nature reviews. Neuroscience 14, 383–400 10.1038/nrn3504 [PubMed: 23686171]

Pettersen EF, Goddard TD, Huang CC, Couch GS, Greenblatt DM, Meng EC, and Ferrin TE (2004). UCSF Chimera - A visualization system for exploratory research and analysis. Journal of Computational Chemistry 25, 1605–1612 10.1002/jcc.20084 [PubMed: 15264254]

Ravikrishnan A, Gandhi PJ, Shelkar GP, Liu J, Pavuluri R, and Dravid SM (2018). Region-specific Expression of NMDA Receptor GluN2C Subunit in Parvalbumin-Positive Neurons and Astrocytes: Analysis of GluN2C Expression using a Novel Reporter Model. Neuroscience 380, 49–62 http://doi.org/10.1016/j.neuroscience.2018.03.011 [PubMed: 29559384]

Regan MC, Grant T, McDaniel MJ, Karakas E, Zhang J, Traynelis SF, Grigorieff N, and Furukawa H (2018). Structural Mechanism of Functional Modulation by Gene Splicing in NMDA Receptors. Neuron 98, 521–529 e523 10.1016/j.neuron.2018.03.034 [PubMed: 29656875]

Regan MC, Romero-Hernandez A, and Furukawa H (2015). A structural biology perspective on NMDA receptor pharmacology and function. Current opinion in structural biology 33, 68–75 10.1016/j.sbi.2015.07.012 [PubMed: 26282925]

Regan MC, Zhu Z, Yuan H, Myers SJ, Menaldino DS, Tahirovic YA, Liotta DC, Traynelis SF, and Furukawa H (2019). Structural elements of a pH-sensitive inhibitor binding site in NMDA receptors. Nat Commun 10, 321 10.1038/s41467-019-08291-1 [PubMed: 30659174]

Romero-Hernandez A, Simorowski N, Karakas E, and Furukawa H (2016). Molecular Basis for Subtype Specificity and High-Affinity Zinc Inhibition in the GluN1-GluN2A NMDA Receptor

Amino-Terminal Domain. Neuron 92, 1324–1336 10.1016/j.neuron.2016.11.006 [PubMed: 27916457]

Salimando GJ, Hyun M, Boyt KM, and Winder DG (2020). BNST GluN2D-Containing NMDA Receptors Influence Anxiety- and Depressive-like Behaviors and ModulateCell-Specific Excitatory/Inhibitory Synaptic Balance. J Neurosci 40, 3949–3968 10.1523/JNEUROSCI.0270-20.2020 [PubMed: 32277042]

Siegler Retchless B, Gao W, and Johnson JW (2012). A single GluN2 subunit residue controls NMDA receptor channel properties via intersubunit interaction. Nat Neurosci 15, 406–413, S401–402 10.1038/nn.3025 [PubMed: 22246434]

Sobolevsky AI, Rosconi MP, and Gouaux E (2009). X-ray structure, symmetry and mechanism of an AMPA-subtype glutamate receptor. Nature 462, 745–756 10.1038/nature08624 [PubMed: 19946266]

Song X, Jensen MO, Jogini V, Stein RA, Lee CH, McHaourab HS, Shaw DE, and Gouaux E (2018). Mechanism of NMDA receptor channel block by MK-801 and memantine. Nature 556, 515–519 10.1038/s41586-018-0039-9 [PubMed: 29670280]

Stroebel D, Buhl DL, Knafels JD, Chanda PK, Green M, Sciabola S, Mony L, Paoletti P, and Pandit J (2016). A Novel Binding Mode Reveals Two Distinct Classes of NMDA Receptor GluN2B-selective Antagonists. Mol Pharmacol 89, 541–551 10.1124/mol.115.103036 [PubMed: 26912815]

Tajima N, Karakas E, Grant T, Simorowski N, Diaz-Avalos R, Grigorieff N, and Furukawa H (2016). Activation of NMDA receptors and the mechanism of inhibition by ifenprodil. Nature 534, 63–68 10.1038/nature17679 [PubMed: 27135925]

Tajima N, Simorowski N, Yovanno RA, Regan MC, Michalski K, Gomez R, Lau AY, and Furukawa H (2022). Development and characterization of functional antibodies targeting NMDA receptors. Nat Commun 13, 923 10.1038/s41467-022-28559-3 [PubMed: 35177668]

Takahashi T, Feldmeyer D, Suzuki N, Onodera K, Cull-Candy SG, Sakimura K, and Mishina M (1996). Functional Correlation of NMDA Receptor ε Subunits Expression with the Properties of Single-Channel and Synaptic Currents in the Developing Cerebellum. The Journal of Neuroscience 16, 4376 10.1523/JNEUROSCI.16-14-04376.1996 [PubMed: 8699248]

Tegunov D, and Cramer P (2019). Real-time cryo-electron microscopy data preprocessing with Warp. Nat Methods 16, 1146–1152 10.1038/s41592-019-0580-y [PubMed: 31591575]

Traynelis SF, Hartley M, and Heinemann SF (1995). Control of proton sensitivity of the NMDA receptor by RNA splicing and polyamines. Science 268, 873–876 [PubMed: 7754371]

Traynelis SF, Wollmuth LP, McBain CJ, Menniti FS, Vance KM, Ogden KK, Hansen KB, Yuan H, Myers SJ, and Dingledine R (2010). Glutamate receptor ion channels: structure, regulation, and function. Pharmacological reviews 62, 405–496 10.1124/pr.109.002451 [PubMed: 20716669]

Vance KM, Simorowski N, Traynelis SF, and Furukawa H (2011). Ligand-specific deactivation time course of GluN1/GluN2D NMDA receptors. Nature communications 2, 294 10.1038/ncomms1295

Wang H, Lv S, Stroebel D, Zhang J, Pan Y, Huang X, Zhang X, Paoletti P, and Zhu S (2021). Gating mechanism and a modulatory niche of human GluN1-GluN2A NMDA receptors. Neuron 109, 2443–2456 e2445 10.1016/j.neuron.2021.05.031 [PubMed: 34186027]

Wang JX, and Furukawa H (2019). Dissecting diverse functions of NMDA receptors by structural biology. Curr Opin Struct Biol 54, 34–42 10.1016/j.sbi.2018.12.009 [PubMed: 30703613]

Wang JX, Irvine MW, Burnell ES, Sapkota K, Thatcher RJ, Li M, Simorowski N, Volianskis A, Collingridge GL, Monaghan DT, et al. (2020). Structural basis of subtype-selective competitive antagonism for GluN2C/2D-containing NMDA receptors. Nat Commun 11, 423 10.1038/s41467-020-14321-0 [PubMed: 31969570]

Yuan H, Hansen KB, Vance KM, Ogden KK, and Traynelis SF (2009). Control of NMDA receptor function by the NR2 subunit amino-terminal domain. J Neurosci 29, 12045–12058 10.1523/JNEUROSCI.1365-09.2009 [PubMed: 19793963]

Zhang JB, Chang S, Xu P, Miao M, Wu H, Zhang Y, Zhang T, Wang H, Zhang J, Xie C, et al. (2018). Structural Basis of the Proton Sensitivity of Human GluN1-GluN2A NMDA Receptors. Cell Rep 25, 3582–3590 e3584 10.1016/j.celrep.2018.11.071 [PubMed: 30590034]

Zhang Y, Ye F, Zhang T, Lv S, Zhou L, Du D, Lin H, Guo F, Luo C, and Zhu S (2021). Structural basis of ketamine action on human NMDA receptors. Nature 10.1038/s41586-021-03769-9

Zhu S, Stein RA, Yoshioka C, Lee CH, Goehring A, McHaourab HS, and Gouaux E (2016). Mechanism of NMDA Receptor Inhibition and Activation. Cell 165, 704–714 10.1016/j.cell.2016.03.028 [PubMed: 27062927]

Zivanov J, Nakane T, and Scheres SHW (2019). A Bayesian approach to beam-induced motion correction in cryo-EM single-particle analysis. IUCrJ 6, 5–17 10.1107/S205225251801463X

Highlights

- The GluN1-2C NMDAR structures show conformational heterogeneity in GluN2C.
- PYD-106 binds to GluN2C in the ‘straight’ conformation.
- GluN1-2A-2C NMDAR contains the GluN2C conformer that is insensitive to PYD-106.
- GluN1a-2D NMDAR has pseudo-symmetry, unlike GluN2C-containing NMDARs.

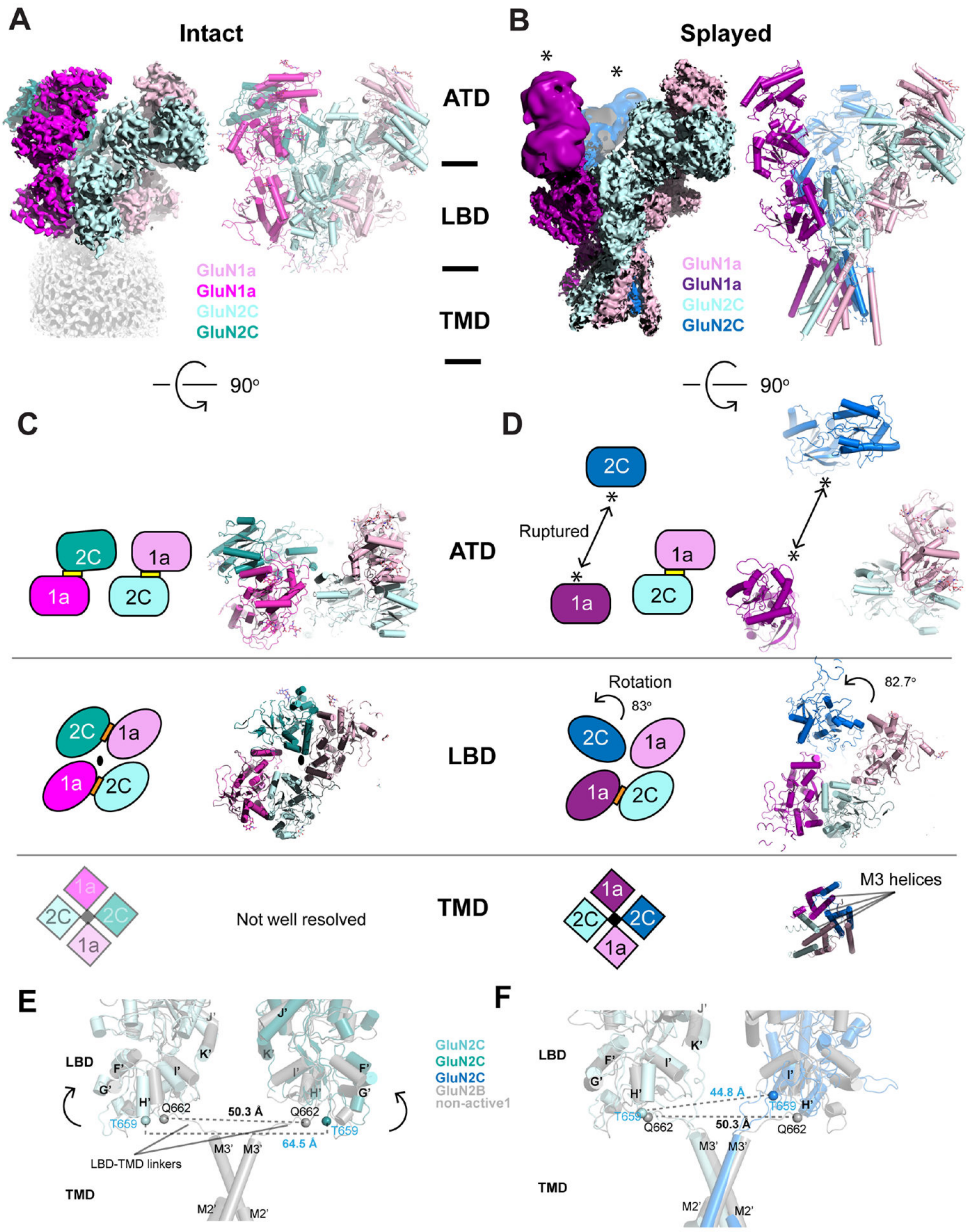

Figure 1. Overall structure of GluN1a-2C NMDAR.

(A and B) GluN1a-2C NMDARs have two major 3D classes, ‘intact (A)’ and ‘splayed (B).’ Cryo-EM density (left) and models (right) are shown in each panel. Asterisks in (B) are representative positions of the highly moving GluN1 and GluN2C ATDs, revealed by focused 3D classification. **(C and D)** Comparisons of ATD, LBD, and TMD layers viewed from the extracellular side. Asterisks in (D) are equivalent to those in (B). Yellow and orange rectangles in the schematics represent the GluN1a-2C heterodimer interfaces in the ATD and LBD layers, respectively. Rupturing of a GluN1a-2C ATD heterodimer leads to a rotation (83°) of one GluN2C LBD. **(E and F)** Comparison of the LBD-TMD linker extension between the ‘intact’ (E) or the ‘splayed’ (F) 3D classes of GluN1a-2C NMDARs and GluN1a-2B NMDARs in the non-active1 conformation (PDB code: 6WHS).

Note that the positions of the two GluN2C LBDs (represented by the distance between Thr659 residues) are more stretched in the ‘intact’ GluN1a-2C NMDARs (64.5 Å) and less stretched in the ‘splayed’ GluN1a-2C NMDARs (44.8 Å) compared to that of the GluN1a-2B NMDARs (represented by the distance between Gln662; 50.3 Å). See also Figure S1, Figure S2, Figure S3, Figure S4, and Table S1.

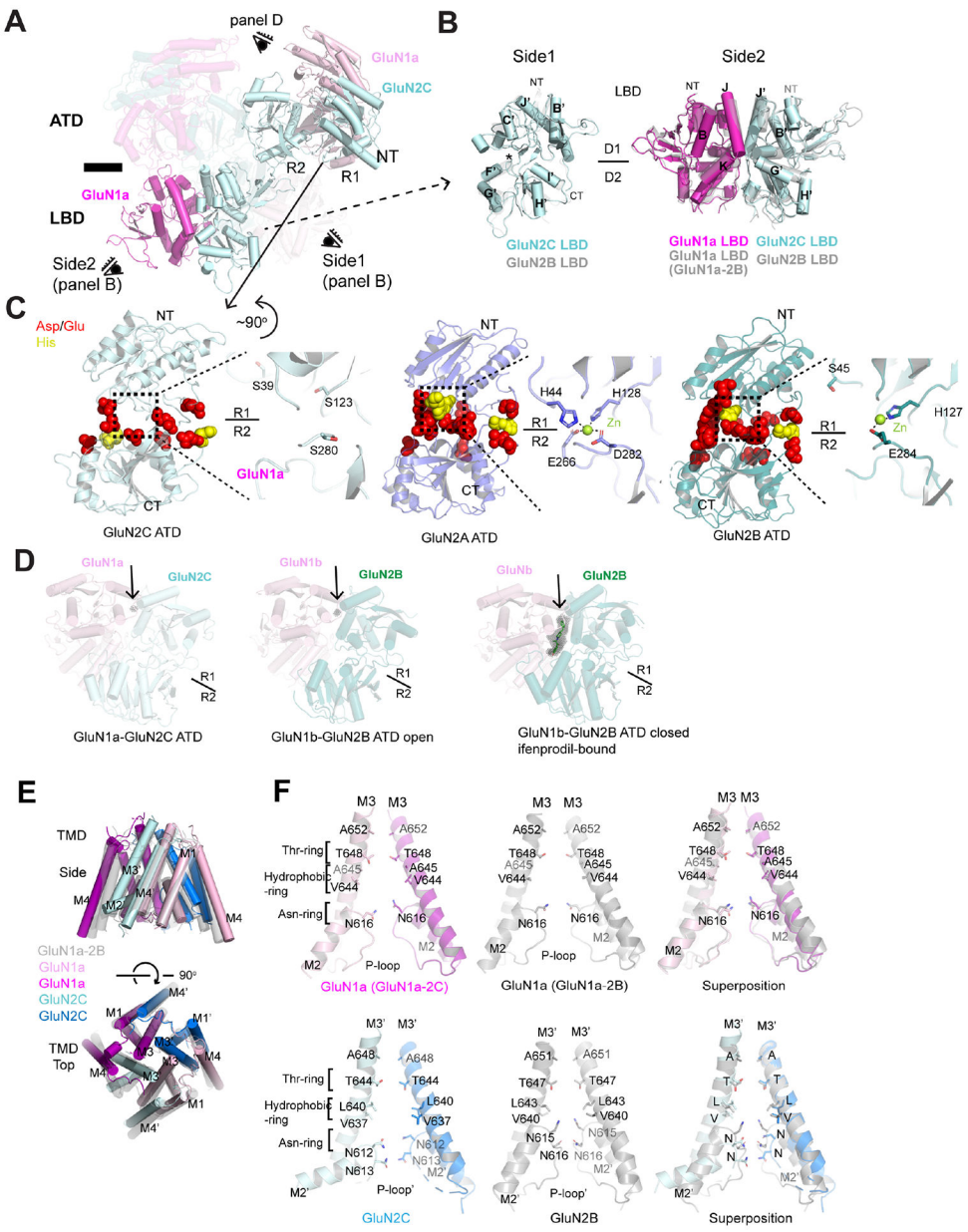

Figure 2. Comparison of domain architectures between different subtypes.

(A) The 'intact' 3D class highlighting one of the two GluN1a-2C ATD and LBD dimers. **(B)** Comparison of GluN2C LBD with GluN2B LBD (PDB code: 7SAA) and the GluN1a-2C LBD dimer with the GluN1a-2B LBD dimer (PDB code: 7SAA) as viewed from side 1 and 2 (eyes in panel A). GluN1a-2C (magenta/cyan) and GluN1a-2B (gray) NMDARs have similar inter-D1-D2 domain orientations and inter-subunit arrangements. **(C)** Comparison of GluN2C ATD with GluN2A and GluN2B ATDs where residues that can control pH sensitivity, Asp/Glu and His, are represented by red and gold spheres, respectively. GluN2C ATD contains no Zn^{2+}-binding residues, as observed in GluN2A and GluN2B ATDs (zoom-in panels). **(D)** The GluN1a-2C ATD dimer interface viewed from the eye in *panel A* and GluN2B ATDs in the open cleft conformation (PDB code: 6WI1) and closed conformation

bound to ifenprodil (PDB code: 3QEL). The mesh represents the solvent accessible volume estimated by KVFinder, demonstrating that the dimer interface in GluN1-2C, like the open conformation of GluN1-2B ATD, does not contain sufficient space for ifenprodil binding. **(E)** Comparison of TMDs from the 'splayed' 3D class of GluN1a-2C and GluN1a-2B NMDARs (gray) viewed from 'side' and 'top.' **(F)** Comparison of the pore-forming M3 helices of the GluN1a (upper panels) and GluN2 (lower panels) between the GluN1a-2C and GluN1a-2B NMDARs. The central pore is partitioned into the Thr-, hydrophobic-, and Asn-rings. While GluN1s are similar, the positions of the Asn-ring residues are different between GluN2A and GluN2C.

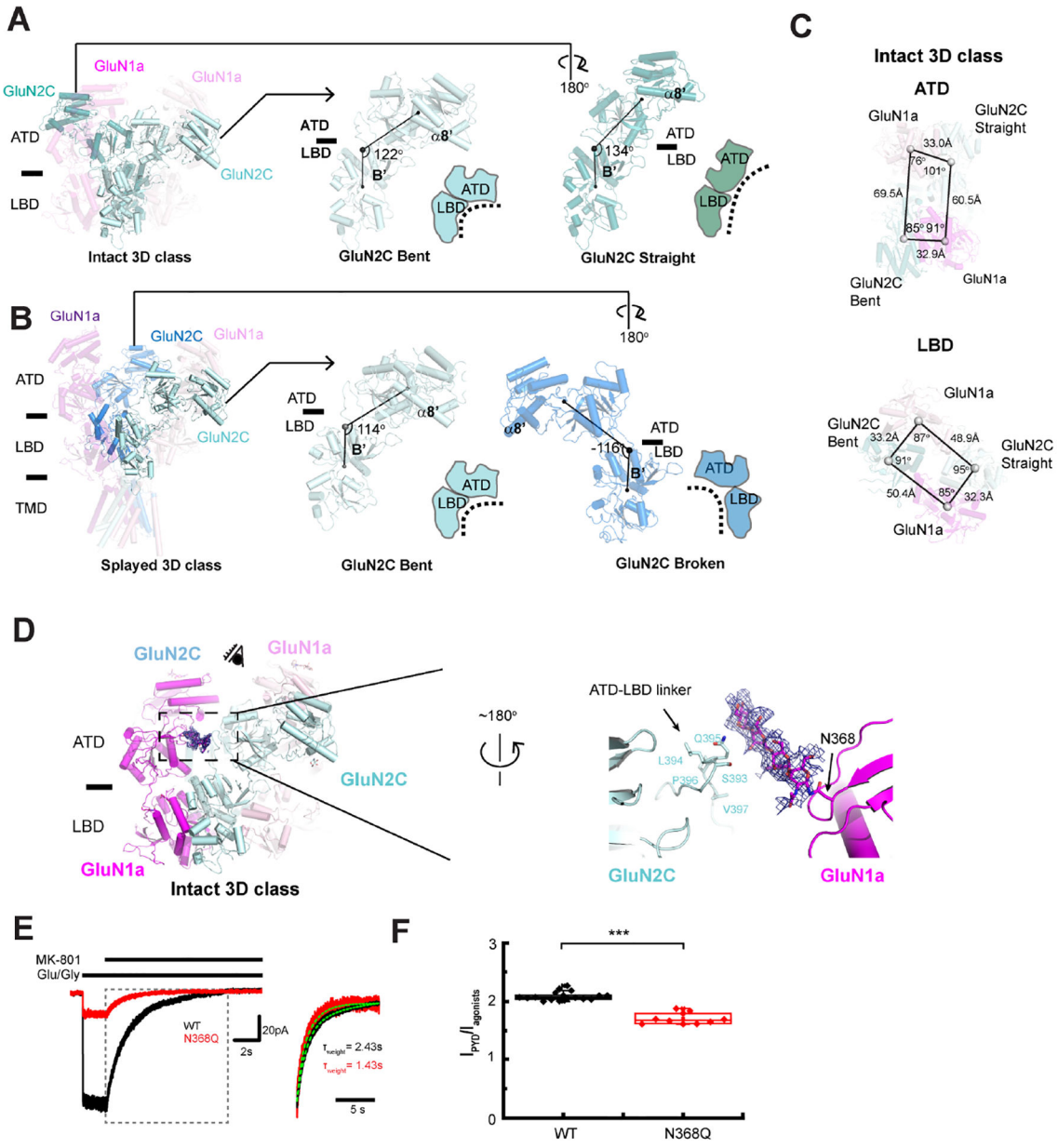

Figure 3. Patterns of ATD-LBD arrangement in GluN2C and inter-subunit interaction.

(A) The ‘intact’ 3D class contains two GluN2Cs with distinct ATD-LBD arrangements, ‘bent’ and ‘straight,’ characterized by the angles formed by the center-of-masses of LBD and ATD and Leu403 Cα (black sphere). **(B)** The ‘splayed’ 3D class contains ‘bent-like’ and ‘broken’ conformers. The ‘bent-like’ conformer a smaller angle than the ‘bent’ in the ‘intact’ 3D class (A). **(C)** The heterogeneous ATD-LBD orientations result in the non-symmetrical arrangement in ATD while the pseudo-C2-symmetrical arrangement is maintained in LBD in the ‘intact’ 3D class. **(D)** The GluN1a-2C NMDAR in the ‘intact’ 3D class and the ordered cryo-EM density for the Asn-linked glycosylation at GluN1a-Asn368. The interaction between the glycosylation chain and the ATD-LBD linker of GluN2C occurs only for the ‘bent’ conformer but not the ‘straight.’ **(E and F)** Removal of the Asn-linked

glycosylation at GluN1a-Asn368 increases the channel open probability as indicated by the faster onset of MK801 **(E)** and lowers PYD-106 potentiation **(F)**. Experiments in (D) are done using a fast solution exchange whole-cell patch-clamp and in (E) are done using TEVC. See also Figure S5.

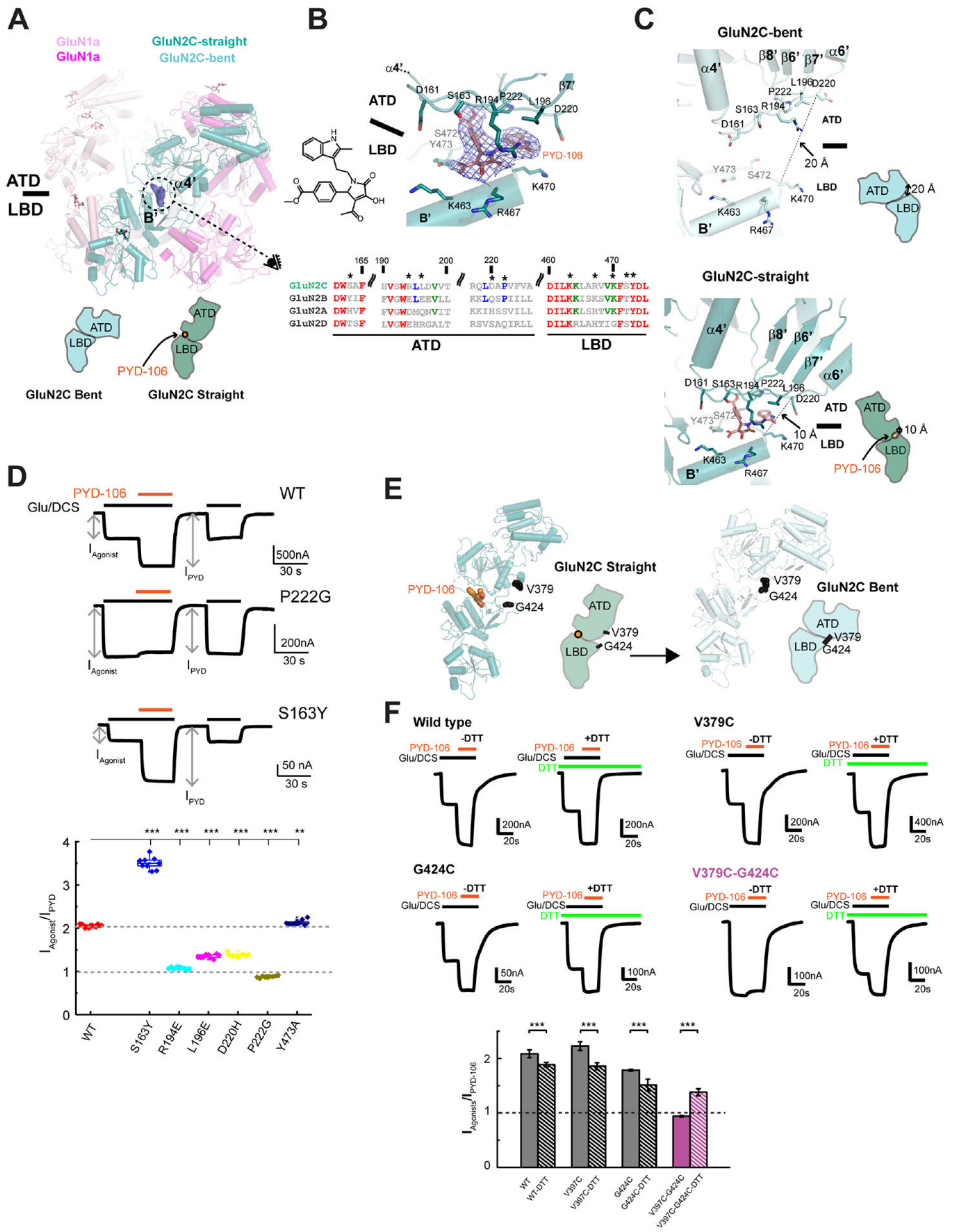

Figure 4. PYD-106 binding site in 'straight' conformation of GluN2C NMDAR.

(A) Cryo-EM density for PYD-106 (blue mesh) was observed only in the GluN2C subunit in the 'straight' conformation. **(B)** The zoom-in view of the binding site from the angle of the 'eye' in *panel A*. The sequence alignment of GluN2A-D where asterisks represent PYD-106 interacting residues. **(C)** Comparison between GluN2C-bent and GluN2C-straight at the PYD-106 binding pocket showing weaker ATD-LBD packing in GluN2C-bent. **(D)** Validation of the PYD-106 binding pocket by site-directed mutagenesis and TEVC. **(E)** Locations of GluN2C-Val379 and -Gly424 at the opposite end of the PYD-106 binding pocket. These residues, when mutated to Cys, would form a disulfide bond only in the 'bent'-GluN2C but not the 'straight'-GluN2C. **(F)** The PYD-106 application for the wildtype, single mutants (Val379 and Gly424), and the double mutant (Val379-Gly424).

Only the double mutant shows no PYD-106 potentiation, which is partially recovered by the breakage of the disulfide bond by a DTT application. Each data point on the bar graph was calculated from the measurement of 4–18 unique oocytes. Error bars represent the average current ± SD. The triple asterisk indicates $P<0.001$ determined by a two-tail *t*-test between the absence and the presence of DTT. See also Figure S2, and Table S1.

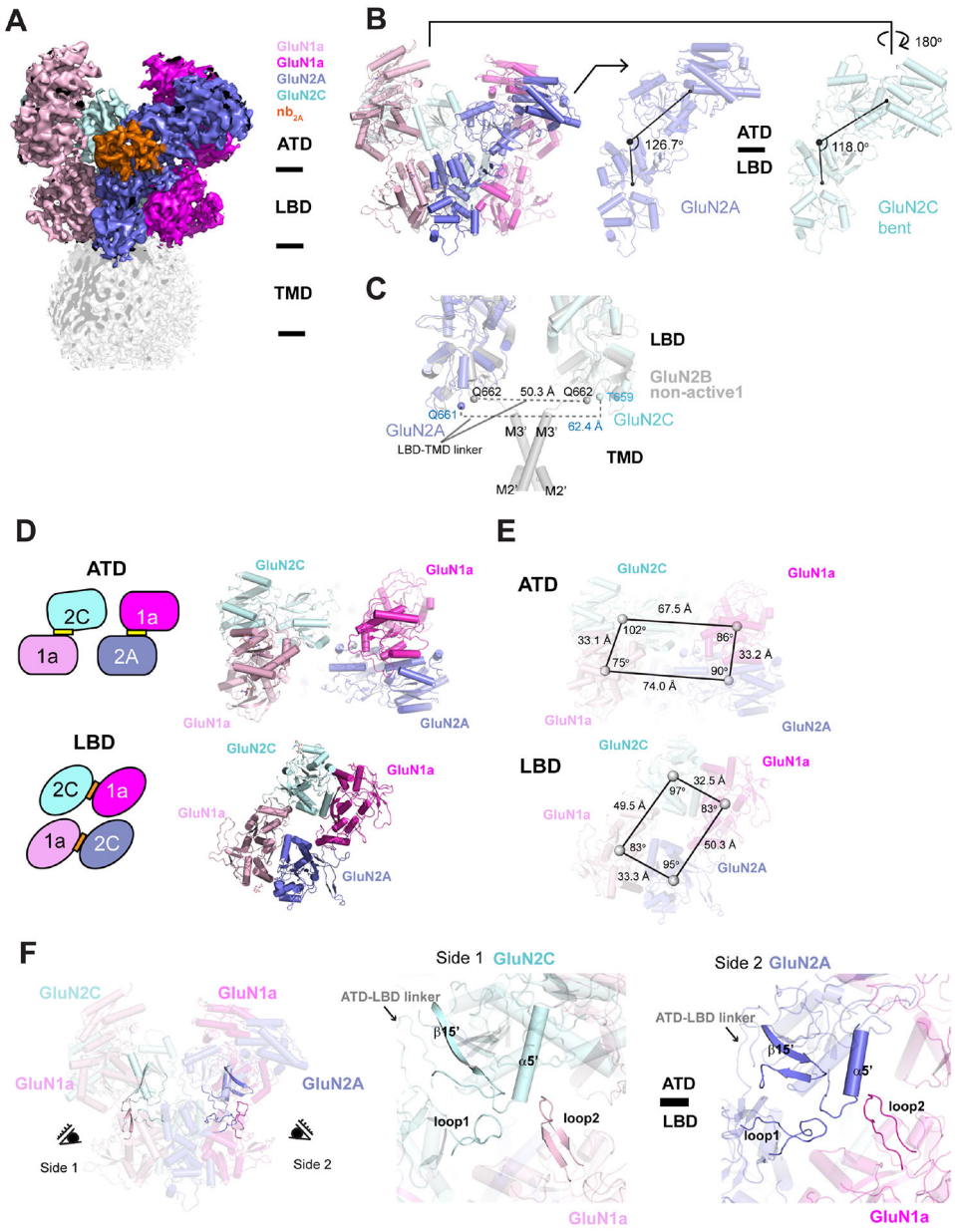

Figure 5. Structure of GluN1a-2A-2C tri-heteromeric NMDAR.

(A) The cryo-EM density of the GluN1a-2A-2C NMDAR. GluN2A was labeled with a nanobody (orange). **(B)** GluN2A and GluN2C in the GluN1a-2A-2C NMDAR are in the 'straight' and 'bent' conformations, respectively. The arrangement between ATD and LBD was estimated as in Figure 3. **(C)** Comparison of the LBD-TMD linker extension between GluN1a-2A-2C NMDAR and GluN1a-2B NMDAR (PDB code: 6WHS; non-active1). The position of the GluN2A and GluN2C LBDs (represented by the distance between GluN2A-Gln661 and GluN2C Thr659; 62.4 Å) is similarly stretched to the one in the 'intact' GluN1a-2C NMDARs (64.5 Å; Figure 1E). **(D and E)** Subunit arrangement in the ATD layer is asymmetrical, whereas that in the LBD layer is pseudo-C2-symmetrical. Yellow and orange rectangles in the schematics represent the GluN1a-2 heterodimer interfaces in the

ATD and LBD layers, respectively. **(F)** GluN2A (Side 2) and GluN2C (Side 1) have distinct loci of inter-domain/subunit interactions involving ATD, LBD, and loop2 of the GluN1 LBD. See also Figure S4, Figure S5, and Table S1.

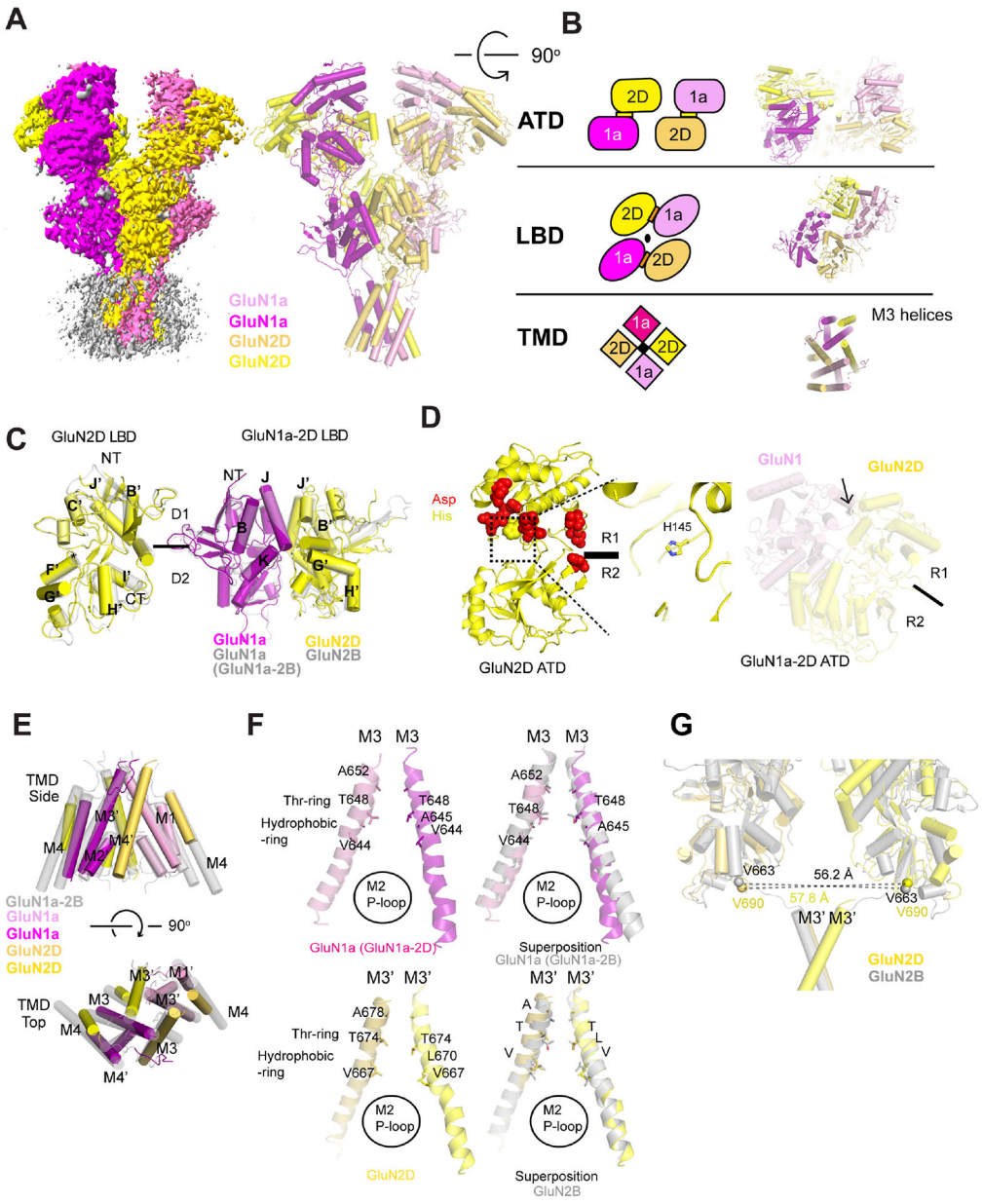

Figure 6. Structure of GluN1a-2D NMDAR.

(A) Cryo-EM density (left) and the models (right) for ATD, LBD, and TMD. **(B)** Comparisons of the ATD, LBD, and TMD layers viewed from the extracellular side. Yellow and orange rectangles in the schematics represent the GluN1a-2D heterodimer interfaces in the ATD and LBD layers, respectively. **(C)** GluN2D ATD where Asp/Glu and His residues are represented by red and gold spheres, respectively (left panel). No Zn^{2+}-binding site is present in the inter-domain cleft (middle panel). The GluN1a-2D ATD dimer interface shows little or no solvent accessible volume estimated by KVFinder (mesh with an arrow; right panel), unlike GluN1-2B ATD, indicating no binding of an allosteric modulator compound in GluN1a-2D ATD. **(D)** Comparison of GluN2D LBD with GluN2B LBD (PDB code: 7SAA; left panel) and the GluN1a-2D LBD with GluN1a-2B LBD (PDB code:

7SAA; right panel). GluN1a-2D (magenta/yellow) and GluN1a-2B (gray) NMDARs have a similar D1-D2 orientation and inter-subunit arrangement. **(E)** Comparison of GluN1a-2D and GluN1a-2B NMDARs TMDs viewed from 'side' and 'top.' **(F)** Comparison of the pore-forming M3 helices of the GluN1a subunit (upper panel) and GluN2 subunit (lower panel) between the GluN1a-2D and GluN1a-2B NMDARs. **(G)** The LBD-TMD linker extension of GluN1a-2D NMDARs and GluN1a-2B NMDARs (PDB code: 7SAA; non-active1). Note that the positions of the two GluN2D LBDs (represented by the distance between Val690 residues) are similar (57.8 Å) compared to that of GluN1a-2B NMDARs (represented by the distance between Val663; 56.2 Å). See also Figure S5, Figure S6, and Table S1.

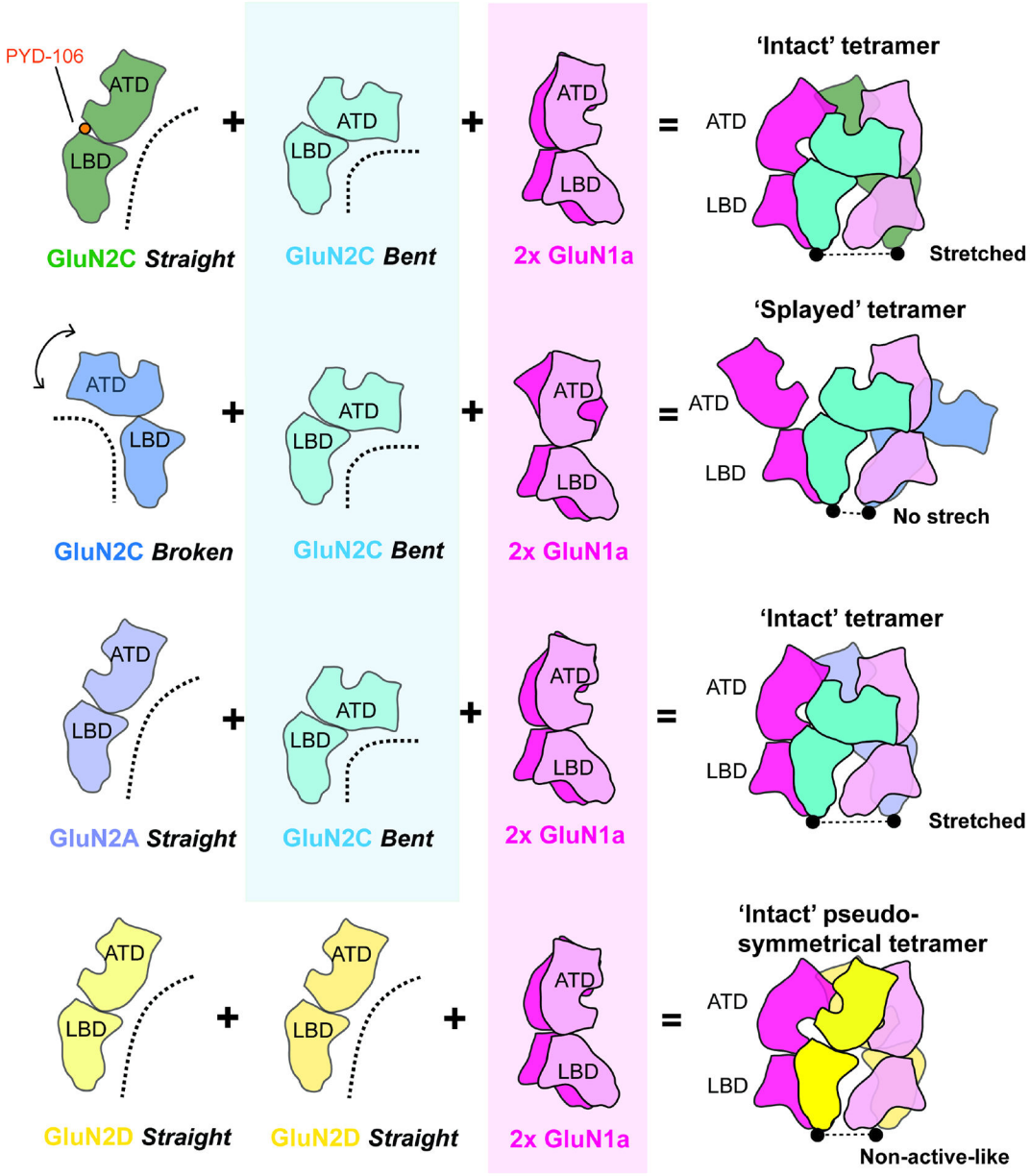

Figure 7. Pattern of subunit assembly in GluN2C- and GluN2D-containing NMDARs.

GluN1a-2C di-heteromeric NMDARs form two types of tetramers, 'intact' and 'splayed,' where the 'intact' likely represents the active conformation as predicted by the 'stretched' distance between the two GluN2C subunits that generates tension for channel gating. A combination of 'straight' and 'bent' GluN2 subunits generates the 'intact' tetramers, whereas that of 'broken' and 'bent' results in the 'splayed' tetramer. PYD-106 specifically binds to the 'straight' conformation of GluN2C, thereby stabilizing the 'intact' tetramer. The 'straight' conformer of GluN2C is replaced by the similarly straight GluN2A in the GluN1a-2A-2C tri-heteromeric NMDAR therefore, the PYD-106 sensitivity is lost. The two

GluN2D subunits in the GluN1a-2D NMDAR have similar conformation, resulting in a pseudo-C2-symmetric tetrameric arrangement.

KEY RESOURCES TABLE

REAGENT or RESOURCE	SOURCE	IDENTIFIER
Chemicals, Peptides, and Recombinant Proteins		
HyClone CCM3 cell culture media	VWR International Inc.	Cat#16777-272
HyClone Leibovitz L-15 Medium	VWR International Inc.	Cat#82024-284
DMEM/GlutaMax medium	GIBCO	Cat#15140-122
Lauryl Maltose Neopentyl Glycol (LMNG)	Anatrace	Cat# NG310
Digitonin	Calbiochem	Cat#300410
D-cycloserine	Sigma-Aldrich	Cat#C6880
Rho 1D4 antibody	University of British Columbia	N/A
1D4 peptide (TETSQVAPA)	ABM	Custom synthesis
Nb-4	Lab stock	N/A
PYD-106	Lab stock (Khatri et al., 2014)	N/A
Experimental Models: Cell Lines		
S. frugiperda, Sf9 cells	Lab stock	N/A
Xenopus laevis (oocyte extraction)	Xenopus1	https://xenopus1.com/
Defolliculated oocytes (*Xenopus laevis*)	Ecocyte	https://ecocyte-us.com/
Human, HEK 293 cells	ATCC	CRL-1573
Deposited Data		
D-cycloserine- and glutamate-bound Human GluN1a-GluN2C NMDA receptor in intact conformation, cryoEM map and molecular model	This study	EMDB: EMD-27953 PDB: 8E92
D-cycloserine- and glutamate-bound Human GluN1a-GluN2C NMDA receptor in splayed conformation, cryoEM map and molecular model	This study	EMDB: EMD-27954 PDB: 8E93
PYD-106-bound Human GluN1a-GluN2C NMDA receptor in intact conformation, cryoEM map and molecular model	This study	EMDB: EMD-27955 PDB: 8E94
PYD-106-bound Human GluN1a-GluN2C NMDA receptor in splayed conformation, cryoEM map and molecular model	This study	EMDB: EMD-27958 PDB: 8E97
D-cycloserine- and glutamate-bound Human GluN1a-GluN2C NMDA receptor in nanodisc - intact conformation, cryoEM map and molecular model	This study	EMDB: EMD-27959 PDB: 8E98
D-cycloserine- and glutamate-bound Human GluN1a-GluN2C NMDA receptor in nanodisc - splayed conformation, cryoEM map	This study	EMDB: EMD-27960
Human GluN1a-GluN2A-GluN2C triheteromeric NMDA receptor in complex with Nb-4, cryoEM map and molecular model	This study	EMDB: EMD-27961 PDB: 8E99
Glycine- and glutamate-bound Human GluN1a-GluN2D NMDA receptor, cryoEM map and molecular model	This study	EMDB: EMD-27957, EMD-28051, EMD-28052, EMD-28053 PDB: 8E96
Recombinant DNA		
Cloning vector: pFp10	Furukawa et al., 2021	Addgene:170460

REAGENT or RESOURCE	SOURCE	IDENTIFIER
Cloning vector: pUCDMp10	Furukawa et al., 2021	Addgene:170461
Cloning vector: pCI-neo	Lab stock	GenBank: U47120.2
HumanGluN1a$_{EM}$	This study	N/A
OS-humanGluN2C$_{EM}$	This study	N/A
OS-humanGluN2C$_{EM}$-P2A-humanGluN2A$_{EM}$-1D4	This study	N/A
OS-humanGluN2D$_{EM}$	This study	N/A
HumanGluN1-4a	This study	N/A
HumanGluN2C	This study	N/A
HumanGluN2D	This study	N/A
Software and Algorithms		
EPU	ThermoFisher	https://www.fei.com/software/epu-automated-single-particles-software-for-life-sciences/
WARP	Tegunov and Cramer, 2019	http://www.warpem.com/warp/
cryoSPARC	Punjani et al., 2017	https://cryosparc.com/
RELION	Zivanov, et al., 2019	https://relion.readthedocs.io/en/release-3.1/
cisTEM	Grant et al., 2018	https://cistem.org/
UCSF Chimera	Oshima et al., 2016	https://www.cgl.ucsf.edu/chimera/
COOT	Emsley et al., 2010	https://www2.mrc-lmb.cam.ac.uk/personal/pemsley/coot/
Phenix	Adams et al., 2010	https://www.phenix-online.org/
Patchmaster	HEKA	https://heka.com/downloads/downloads_main.html#down_patchmaster
Origin	OriginLab Corp	https://www.originlab.com/
ChemDraw	PerkinElmer	https://www.perkinelmer.com/category/chemdraw
Pymol	Schrodinger	https://pymol.org/2/
Clampex	Molecular Devices	https://www.moleculardevices.com/#gref
ChannelLab	Synaptosft	N/A
Other		
Strep-Tacin Sepharose resin	IBA Lifescience	Cat#2-1201-025
Superose 6 Increase column 10/300 GL	GE Healthcare	Cat#29091596
UltrAUfoil gold grids	Electron Microscopy Sciences	Cat#Q350AR1.3A
Quantifoil R1.2/1.3 copper grids	Electron Microscopy Sciences	Cat#Q450CR1.3